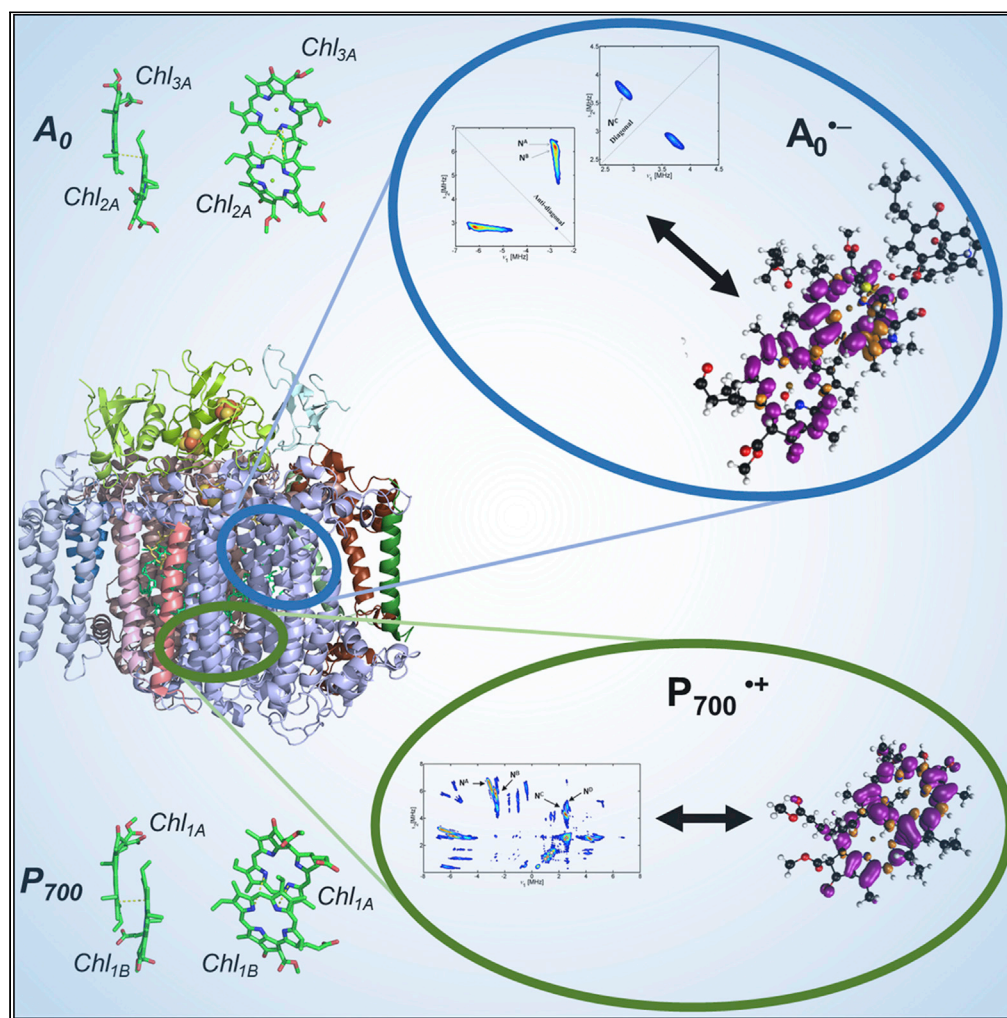**Article**

A dimeric chlorophyll electron acceptor differentiates type I from type II photosynthetic reaction centers

Michael Gorka, Philip Charles, Vidmantas Kalendra, Amgalanbaatar Baldansuren, K.V. Lakshmi, John H. Golbeck

lakshk@rpi.edu (K.V.L.)
jhg5@psu.edu (J.H.G.)

Highlights

Electron-nuclear hyperfine couplings indicate that $A_0^{\cdot-}$ is a chlorophyll dimer

DFT calculations reveal electron delocalization over both Chl_2 and Chl_3 in $A_0^{\cdot-}$

Photosystem I utilizes Chl dimers as both the primary donor (P_{700}) and acceptor (A_0)

A_0 is predicted to be a dimer in type I RCs and a monomer in type II RCs

iScience

Article

A dimeric chlorophyll electron acceptor differentiates type I from type II photosynthetic reaction centers

Michael Gorka,[1] Philip Charles,[2] Vidmantas Kalendra,[2] Amgalanbaatar Baldansuren,[2] K.V. Lakshmi,[2,4,*] and John H. Golbeck[1,3,*]

SUMMARY

This research addresses one of the most compelling issues in the field of photosynthesis, namely, the role of the accessory chlorophyll molecules in primary charge separation. Using a combination of empirical and computational methods, we demonstrate that the primary acceptor of photosystem (PS) I is a dimer of accessory and secondary chlorophyll molecules, Chl_{2A} and Chl_{3A}, with an asymmetric electron charge density distribution. The incorporation of highly coupled donors and acceptors in PS I allows for extensive delocalization that prolongs the lifetime of the charge-separated state, providing for high quantum efficiency. The discovery of this motif has widespread implications ranging from the evolution of naturally occurring reaction centers to the development of a new generation of highly efficient artificial photosynthetic systems.

INTRODUCTION

Nature powers present day Earth with oxygenic photosynthesis. In this highly evolved process, solar energy is used to convert carbon dioxide and water into carbohydrates, releasing dioxygen into the atmosphere as a byproduct. Chlorophyll (Chl) molecules are central to oxygenic photosynthesis as they participate in both energy and electron transfer (ET) (Rabinowitch and Govindjee, 1965; Thornber, 1975; Katz et al., 1978; Anderson, 1982). While there are a wide variety of Chls in nature that absorb light in different regions of the visible and near-IR spectrum, the arrangement and function of Chls are conserved in reaction center (RC) proteins across different species of photosynthetic organisms (Olson and Pierson, 1987; Meyer, 1994; Orf et al., 2018; Chen et al., 2020). The type I photosynthetic RC, photosystem (PS) I (Figure 1A), in cyanobacteria consists of approx. 96 peripheral Chl a molecules (Jordan et al., 2001). Additionally, the heterodimeric core of PS I, which comprised the PsaA and PsaB polypeptides, contains three Chl a molecules ($Chl_{1A/1B}$, $Chl_{2A/2B}$ and $Chl_{3A/3B}$) in the pseudo-symmetric A and B branch of cofactors (Figure 1B) (Fromme et al., 2001; Jordan et al., 2001). ET in PS I is initiated when the antenna Chl absorb light and transfer the excitation energy with high quantum efficiency to two electronically coupled Chl_{1A} and Chl_{1B} molecules known as the primary donor, P_{700} (Şener et al., 2011). The photoexcited P_{700}^* state leads to rapid ET, resulting in the formation of the first detectable charge-separated state, $P_{700}^{\cdot+}A_{0A}^{\cdot-}$ or $P_{700}^{\cdot+}A_{0B}^{\cdot-}$, respectively (Wasielewski et al., 1987; Shelaev et al., 2010; Chauvet et al., 2012; Milanovsky et al., 2014). Both branches are active in PS I; however, the A-branch is preferred over the B-branch by a factor of ~2 in cyanobacteria (Dashdorj et al., 2005). The initial charge separation is stabilized by forward ET to a low-potential phylloquinone, A_{1A} or A_{1B} (Deligiannakis et al., 1998; Ishikita and Knapp, 2003; van der Est, 2006; Srinivasan and Golbeck, 2009), with ET along the A- and B-branches converging at the [4Fe–4S] cluster, F_X. Subsequently, the electron is transferred serially through the terminal [4Fe–4S] clusters, F_A and F_B, in the PsaC polypeptide (Golbeck, 2006) (Figure 1B) which results is the generation of reducing equivalents that are stored as NADPH for use in the carbon fixation reactions.

While the kinetics and thermodynamics of each ET step beyond A_0 are well characterized (Kurashov et al., 2018; Ptushenko et al., 2008; Srinivasan and Golbeck, 2009), less is known about the mechanism of charge separation and the electronic structure of the $A_{0A/0B}^{\cdot-}$ state. Early research on PS I led to differing models of the reduced primary acceptor, $A_{0A/0B}^{\cdot-}$. Picosecond optical spectroscopic studies revealed shifts in the absorbance features at 695 nm that suggested the primary acceptor was Chl a dimer (Shuvalov et al.,

[1]Department of Biochemistry and Molecular Biology, The Pennsylvania State University, University Park, PA 16802, USA

[2]Department of Chemistry and Chemical Biology and The Baruch '60 Center for Biochemical Solar Energy Research, Rensselaer Polytechnic Institute, Troy, NY 12180, USA

[3]Department of Chemistry, The Pennsylvania State University, University Park, PA 16802, USA

[4]Lead contact

*Correspondence:
lakshk@rpi.edu (K.V.L.),
jhg5@psu.edu (J.H.G.)
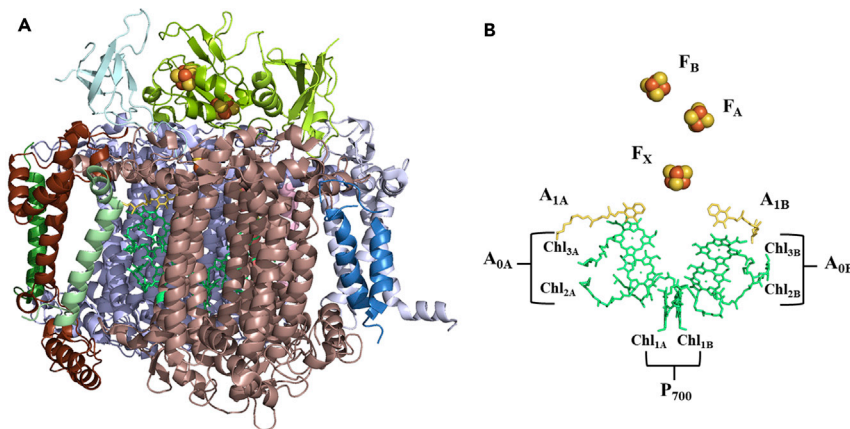https://doi.org/10.1016/j.isci.2021.102719

Figure 1. Crystal structure of photosystem I and electron transfer cofactors
The (A) polypeptide subunits and (B) electron transfer cofactors as observed in the 2.5 Å resolution X-ray crystal structure of cyanobacterial PS I (Jordan et al., 2001). The core subunits, PsaA, PsaB, and PsaC are displayed as salmon, purple, and green ribbons, respectively. Electron transfer cofactors are denoted with the commonly accepted spectroscopic labels, as well as crystallographic labels, for the six Chl cofactors.

1979a, 1979b, 1979c). Subsequently, analysis of EPR line widths and electron nuclear double resonance (ENDOR) data concluded that the line width of the reduced primary acceptor was too large for a dimeric complex, instead suggesting the acceptor was better described as monomeric Chl a molecule (Fajer et al., 1980; Forman et al., 1981). The high-resolution X-ray crystal structure has established that there are three distinct pairs of Chl a molecules, $Chl_{1A/1B}$, $Chl_{2A/2B}$ and $Chl_{3A/3B}$, in the central core of cyanobacterial PS I (Fromme et al., 2001; Jordan et al., 2001). $Chl_{1A/1B}$ are in close proximity, providing confirmation that P_{700} functions as a heterodimer of Chl a/Chl a' molecules (Figures 4C and 4D). Interestingly, $Chl_{2A/3A}$ and $Chl_{2B/3B}$ are oriented in a similar fashion to P_{700} (Figures 4A and 4B), and while they have slightly longer inter-cofactor distances, their structure could allow for the possibility of a dimeric complex.

It is important to note that while the spatial orientation of the $Chl_{1A/1B}$ and $Chl_{2A/2B}$/$Chl_{3A/3B}$ molecules are similar, there are important differences in their respective ligand environments. The Mg^{2+} ion of $Chl_{1A/1B}$ is axially coordinated by a nitrogen atom of a histidine residue ($His680_{PsaA}$ and $His660_{PsaB}$), whereas $Chl_{2A/2B}$ and $Chl_{3A/3B}$ are coordinated to a water ligand and soft base sulfur ligand from a methionine residue ($Met688_{PsaA}$ and $Met668_{PsaB}$), respectively (Jordan et al., 2001). The latter is not predicted by the normative rules of inorganic chemistry (Pearson, 1963; Ayers, 2005), as the central Mg^{2+} ion of Chl a is a relatively hard acid that is usually coordinated to hard nitrogen (and sometimes oxygen) ligands. In contrast, a sulfur ligand is a highly polarizable soft Lewis base. This suggests that the axial coordination of the central Mg^{2+} ion could be instrumental in achieving a low midpoint potential that is necessary for establishing extremely rapid charge separation within ~100 fs of photoexcitation (Shelaev et al., 2010). It is therefore not surprising that replacement of the axial Met ligand with a harder base (His) displays profound effects on the rates and efficiency of ET in both branches (Sun et al., 2014). Additional mutations to this ligand (Xu et al., 2003a, 2003b; Cohen et al., 2004; Dashdorj et al., 2005; Savitsky et al., 2009) and to the hydrogen (H-) bonded tyrosine residue (Li et al., 2006) have been shown to alter ET, but they have not fully elucidated the nature of the $A_0^{\cdot -}$ state.

P_{700} functions as the primary electron donor (Brettel and Leibl, 2001), but to date, the role of the $Chl_{2A/2B}$ cofactor, which is located within a center-to-center distance of ~8 Å of $Chl_{3A/3B}$, remains unclear (Figure 1B) (Jordan et al., 2001), and several compelling models have been put forward in recent years. Ultra-fast transient absorption spectroscopy on genetic variants of PS I isolated from *Chlamydomonas reinhardtii* containing changes in the protein environment surrounding the $Chl_{2A/2B}$ and $Chl_{3A/3B}$ cofactors have suggested that charge separation may be initiated within this pair, after which the hole is rapidly re-reduced by P_{700} (Müller et al., 2003, 2010; Holzwarth et al., 2006). Other studies, however, have argued that the redox potentials of $Chl_{2A/2B}$ and $Chl_{3A/3B}$ would make initial charge separation from this pair thermodynamically unfavorable (Ptushenko et al., 2008). Instead, it has been suggested that the short distance and redox potential difference between $Chl_{2A/2B}$ and $Chl_{3A/3B}$ could allow them to function as a pseudo-dimer,

asymmetrically sharing electron spin density in a ratio of approximately $Chl_{2A/2B}:Chl_{3A/3B}::1:7$ in the initial charge separated state (Ptushenko et al., 2008). Yet others suggest that these six Chl a molecules that comprise the core of PS I are electronically coupled (Gibasiewicz et al., 2003; Yin et al., 2007; Cherepanov et al., 2020).

Cherepanov et al. (Cherepanov et al., 2020) recently proposed that the primary donor Chl, $Chl_{1A/1B}$, and the nearest Chl, $Chl_{2A/2B}$, are combined in a unified exciplex, $(Chl_{2A}Chl_{1A}Chl_{1B}Chl_{2B})$. Using femtosecond pump-probe spectroscopy, they demonstrated that the excitation of the exciplex led to the formation of an excited state, $(Chl_{2A}Chl_{1A}Chl_{1B}Chl_{2B})^*$, that was mixed with two charge-transfer states $P_{700}^{\cdot+}Chl_{2A}^{\cdot-}$ and $P_{700}^{\cdot+}Chl_{2B}^{\cdot-}$. The negative charge was predominantly localized on $Chl_{2A/2B}$ and subsequently, dielectric polarization of the protein further localized the charge on $Chl_{3A/3B}$. It was suggested that the electron density was subsequently redistributed between the A- and B-branch that largely generated the $A_{1A}^{\cdot-}$ state. However, empirical evidence has been insufficient to determine the precise role of $Chl_{2A/2B}$ and its interaction with $Chl_{3A/3B}$ in the charge-separated state, $P_{700}^{\cdot+}A_0^{\cdot-}$.

Continuous-wave (CW) and pulsed electron paramagnetic resonance (EPR) spectroscopy have been employed to study the molecular structure and function of the Chl cofactors (Commoner et al., 1956; Käβ et al., 1995, 1996; Käβ and Lubitz, 1996). These methods have made it possible to probe the unpaired electron spin that is formed upon photo-oxidation or reduction of Chl in photosynthetic RCs. In fact, one of the earliest applications of EPR spectroscopy by Commoner et al. detected the steady-state photoaccumulation of the primary donor cation, $P_{700}^{\cdot+}$, of PS I (Commoner et al., 1956). Subsequently, the signal was attributed to a strongly electronically coupled Chl a dimer (Chl_{1A} and Chl_{1B} in Figure 1B) (Norris et al., 1971; Davis et al., 1993; Mac et al., 1998; Käss et al., 2001), given that the line width was narrower than that of a monomeric Chl a (Norris et al., 1971). It was shown that the relationship, $\Delta H_N = 1/\sqrt{N} \cdot \Delta H_M$ (where ΔH_N and ΔH_M are the line width of the multimeric Chl cation with spin delocalization, $Chl_N^{\cdot+}$, and monomeric $Chl^{\cdot+}$ cation, respectively), accounted for the delocalization of the unpaired electron spin over the dimeric $Chl_{1A/1B}$ cofactors of $P_{700}^{\cdot+}$ (Norris et al., 1971). More recently, pulsed EPR methods, such as, transient EPR, ENDOR, and electron spin echo envelope modulation (ESEEM) spectroscopy along with computational modeling have provided a wealth of information on the rates of ET and the electronic structure of the cofactors of PS I (Mac et al., 1996, 1998; Käss et al., 2001; Deligiannakis and Rutherford, 2001; Srinivasan et al., 2009, 2011a, 2011b; Poluektov et al., 2005; Norris et al., 1974) and other RCs (Deligiannakis et al., 1999; Lubitz et al., 2002; Britt et al., 2004; Schnegg et al., 2007).

While CW and pulsed EPR spectroscopy of the Chl $a^{\cdot-}$ anion *in vitro* have provided initial models for the A_0 acceptor of PS I (Hoff et al., 1982; Rigby et al., 2003), the precise electronic structure of $A_0^{\cdot-}$ has yet to be determined *in vivo*. In certain cases, *in vitro* studies can serve as adequate models for *in vivo* Chl molecules, but in the case of A_0, these lack the smart matrix effects of the protein environment that influence its function. The 2.5 Å resolution X-ray crystal structure of PS I (Jordan et al., 2001) sets the stage for the application of state-of-the-art experiments and theory to interrogate the molecular and electronic structure of A_0 within the protein. In this work, we utilize a combination of two-dimensional (2D) hyperfine sublevel correlation (HYSCORE) spectroscopy and density functional theory (DFT) to probe the electronic structure of the primary acceptor, $A_0^{\cdot-}$. The paramagnetic $A_0^{\cdot-}$ state of PS I is uniquely poised to provide information on the electron-nuclear hyperfine interactions with constituent ^1H and ^{14}N atoms. HYSCORE spectroscopy is ideally suited for this study as it provides enhanced resolution from the detection of the hyperfine signals in 2D space, which alleviates the problem of spectral overcrowding from the signals of multiple ^1H and ^{14}N atoms present in the $A_0^{\cdot-}$ state (Harmer et al., 2009). Additionally, the nuclear transitions are correlated in the two dimensions, which greatly simplifies the analysis and interpretation of the spectra. We have previously demonstrated the application of 2D ^1H and ^{14}N HYSCORE to determine the strength and orientation of H-bonds of the quinone cofactors of PS I and PS II that provided insight on the role of H-bonds in the tuning of the midpoint potential of the quinone acceptors (Chatterjee et al., 2011; Srinivasan et al., 2011a).

In conjunction with 2D ^{14}N and ^1H HYSCORE measurements of the $A_0^{\cdot-}$ state, we performed advanced DFT calculations on an extensive computational model of PS I that includes the $Chl_{1A/1B}$, $Chl_{2A/2B}$, Chl_{3A}, and A_{1A} cofactors with all of the associated amino acid and water ligands. This allowed us to model the effects of the unusual axial coordination of the Chl, H-bonding interactions and proximity effects from the cofactors in the A-branch of PS I. This combination of experiment and theory has led to the first direct determination of electron delocalization over the Chl_{2A} and Chl_{3A} dimer in the $A_0^{\cdot-}$ state, which was previously
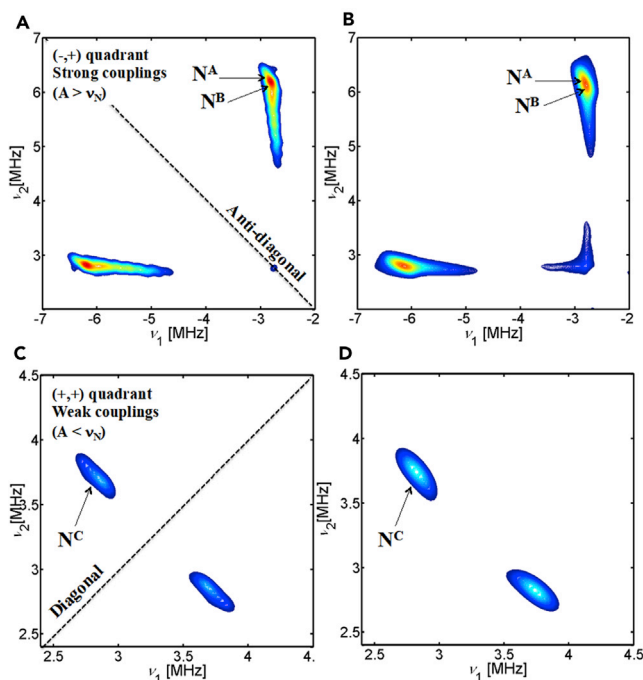
Figure 2. Experimental and simulated 2D ^{14}N HYSCORE spectra of the $A_0^{\cdot-}$ state

(A and C) Experimental and (B and D) simulated 2D ^{14}N HYSCORE spectra of the $A_0^{\cdot-}$ state of PS I. The cross-peaks in the (−,+) and (+,+) quadrant that are centered at multiples of the ^{14}N Zeeman frequency (ν_N of 1.07 MHz) arise from the hyperfine interactions of the unpaired electron spin with three nitrogen-14 atoms (nuclear spin, I = 1), $N^A - N^C$. Figures S1, S2, and S4 display the field-sweep electron-spin-echo spectrum, complete HYSCORE spectrum and a detailed simulation of the (−,+) quadrant of the HYSCORE spectrum of the $A_0^{\cdot-}$ state, respectively. The complete set of simulation parameters for the spectra in part (A) and (B) and the calculated hyperfine and quadrupolar couplings are presented in Tables S1 and S4, respectively.

believed to be a monomeric Chl electron acceptor. The uncovering of a dimeric Chl motif in the $A_0^{\cdot-}$ state has widespread implications ranging from the evolution of RCs in natural photosynthesis to the development of a new generation of bio-inspired artificial photosynthetic systems.

RESULTS

Two-dimensional HYSCORE spectroscopy reveals electron spin delocalization in the $A_0^{\cdot-}$ state

Cryogenic illumination of PS I in which forward ET to A_1 is inhibited and the FeS clusters are reduced leads to the photoaccumulation of the $A_0^{\cdot-}$ state. While the field-sweep electron-spin-echo signal indicates the presence of an unpaired electron spin, S, of $^1/_2$ (Figure S1), the weak electron-nuclear hyperfine interactions of the electron spin with the surrounding magnetic nuclei are not resolved in the X-band $A_0^{\cdot-}$ spectrum. In comparison, the 2D HYSCORE spectrum clearly displays two sets of distinct cross-peaks centered at 3–4 MHz and 14.7 MHz that arise from the hyperfine interactions of the unpaired electron spin with the proximal nitrogen-14 (^{14}N, nuclear spin of I = 1) and hydrogen (^1H, I = $^1/_2$) atoms of the $A_0^{\cdot-}$ state, respectively (Figure S2). The ^{14}N and ^1H cross-peaks are separated in frequency space due to a large difference in their respective gyromagnetic ratios (γ) (19.3 × 10^6 and 267.5 × 10^6 rad·s^{-1}·T^{-1} for ^{14}N and ^1H, respectively). For the purpose of this study, we will focus on the ^{14}N hyperfine interactions of the $A_0^{\cdot-}$ state (see supplemental information for a description of the ^1H hyperfine interactions (Figure S3)).

The cross-peaks in the experimental and simulated 2D ^{14}N HYSCORE spectrum of the $A_0^{\cdot-}$ state in Figures 2A–2D and S4 arise from hyperfine interactions with three ^{14}N atoms, labeled $N^A - N^C$. Typically, the spectral features from ^{14}N atoms that are strongly hyperfine-coupled to the unpaired electron spin (A > 2ν_N, where A is the hyperfine coupling constant) lead to cross-peaks in the (−,+) quadrant of the spectrum, while those from the weakly coupled ^{14}N atoms (A < 2ν_N) are observed in the (+,+) quadrant (Höfer et al., 1986).

Table 1. Experimentally determined hyperfine and quadrupolar parameters of ^{14}N atoms in the $A_0^{\cdot-}$ state

Nitrogen	A_{iso} [MHz]	K [MHz]	η	Ring nitrogen	A_{iso} [MHz][a]	A_{iso} [MHz][b]	A_{iso} [MHz][c]
N^A	2.8 ± 0.2	0.69 ± 0.02	0.45 ± 0.2	N^1 (Chl$_{3A}$)	5.50	5.2	5.16
N^B	2.73 ± 0.2	0.69 ± 0.02	0.45 ± 0.2	N^2 (Chl$_{3A}$)	4.44	8.7	6.42
N^C	0.52 ± 0.2	0.69 ± 0.02	0.45 ± 0.2	N^{2-3} (Chl$_{2A}$)	(−)2.03	1.7	<2
N^D	–	–	–		(−)0.55	0.8	<2

Experimental ^{14}N isotropic hyperfine (A_{iso}), quadrupolar (K) and asymmetry (η) parameters of the $A_0^{\cdot-}$ state of PS I obtained from the 2D ^{14}N HYSCORE spectroscopy measurements. Also shown are comparisons of A_{iso} values obtained from isolated monomeric Chl $a^{\cdot-}$ and Pheo$^{\cdot-}$ anions in vitro, as well as Pheo$^{\cdot-}$ measured in PS II. The complete set of simulation parameters for the experimental spectra and calculated hyperfine and quadrupolar couplings are presented in Tables S1 and S4, respectively.
[a]Monomeric Chl $a^{\cdot-}$ anion in vitro(Hoff et al., 1982).
[b]ESEEM measurements of Pheo$^{\cdot-}$ in PS II(Deligiannakis and Rutherford, 1997).
[c]^{14}N-ENDOR measurements of monomeric Pheo$^{\cdot-}$ in vitro(Lendzian et al., 1982).

Thus, the pair of overlapping cross-peaks at (−6.2, 2.8) MHz that are well-pronounced, intense, and symmetric about the anti-diagonal in the (−,+) quadrant of the spectrum in Figure 2A are identified as double quantum correlations of ^{14}N atoms, N^A and N^B, that are strongly coupled to the unpaired electron spin of $A_0^{\cdot-}$. The separation between the cross-peaks is nearly four times the corresponding ^{14}N Zeeman frequency ($ν_N$ of 1.07 MHz). In contrast, there is a single pair of cross-peaks at a frequency of (2.85, 3.7) MHz in the (+,+) quadrant of the spectrum in Figure 2B that is symmetric about the diagonal. These cross-peaks arise from the weakly hyperfine-coupled ^{14}N atom(s), N^C. In each case, the small shift along the diagonal from multiples of the ^{14}N Zeeman frequency, $ν_N$, is due to the nuclear quadrupolar interaction of the nitrogen atoms.

The cross-peaks for $N^A - N^C$ facilitate the determination of the quadrupolar and hyperfine parameters through numerical simulations of the experimental spectra (Tables 1 and S1). Each set of cross-peaks is uniquely defined by the isotropic hyperfine coupling constant or Fermi contact term, A_{iso}, anisotropic dipolar hyperfine interaction, T, quadrupolar coupling constant, K, and asymmetry parameter, η. The isotropic hyperfine coupling constant or Fermi contact term, A_{iso}, provides a measure of the electron spin density at the nucleus, while T reflects the dipole-dipole interaction between the electron and nuclear spin. Additionally, for ^{14}N (nuclear spin I of 1) the quadrupolar coupling and asymmetry parameter, K and η, are valuable probes of the chemical nature and electric field gradient of a quadrupolar nucleus. The quadrupolar coupling constant, K, for all of the hyperfine-coupled nitrogen atoms ($N^A - N^C$) is identical, indicating a similar chemical bonding environment (Tables 1 and S1). Moreover, the K value of 0.69 ± 0.02 MHz reveals that $N^A - N^C$ are pyrrole nitrogen atoms of a Chl ring (Deligiannakis et al., 2000; García-Rubio et al., 2003; van Doorslaer, 2017; Charles et al., 2020). Interestingly, the value of the isotropic hyperfine constant, A_{iso}, for $N^A - N^C$ ranges from 2.8–0.52 MHz, indicating that the spin density of the unpaired electron is distributed on at least three of the constituent nitrogen atoms in the $A_0^{\cdot-}$ state, albeit to different extents. Additionally, the A_{iso} of $N^A - N^C$ for $A_0^{\cdot-}$ is smaller than the hyperfine couplings that were previously observed for the nitrogen atoms of both the monomeric Chl $a^{\cdot+}$ cation (Deligiannakis and Rutherford, 2001) and Chl $a^{\cdot-}$ anion (Hoff et al., 1982) in vitro.

Electron-nuclear hyperfine parameters of the $A_0^{\cdot-}$ state are similar to the $P_{700}^{\cdot+}$ state

For a direct comparison with a paramagnetic Chl species in vivo, we measured the CW (Figure S6) and 2D ^{14}N HYSCORE spectrum of the primary donor cation, $P_{700}^{\cdot+}$, of PS I (Figures S7 and S8). We observed multiple cross-peaks in the (−,+) and (+,+) quadrant of the spectrum that arise from strongly and weakly hyperfine-coupled ^{14}N atoms, respectively. The hyperfine and quadrupolar coupling parameters from numerical simulations (Figures S7B, S7C, S8B, and S8C) of the experimental spectra (Figure S7A and S8A) are presented in Table S2. There are at least four distinct ^{14}N atoms, $N^A - N^D$, (and likely more than four nitrogen atoms if we consider the possibility of overlapping cross-peaks in the (+,+) quadrant that arise from weak hyperfine couplings of 0.4–0.5 MHz) that are interacting with the unpaired electron spin (S = 1/2) on the primary donor cation, $P_{700}^{\cdot+}$. Similar to the $A_0^{\cdot-}$ state, the K value of 0.69 ± 0.2 MHz indicates that $N^A - N^D$ are pyrrole nitrogen atoms in $P_{700}^{\cdot+}$ (Deligiannakis et al., 2000; García-Rubio et al., 2003; van Doorslaer, 2017; Charles et al., 2020). The most pertinent parameter, A_{iso}, ranges from 1.4–2.8 MHz, indicating that the electron spin is distributed on at least four nitrogen atoms in $P_{700}^{\cdot+}$ (Deligiannakis and Rutherford, 2001). Once

again, the A_{iso} values of $P_{700}^{\cdot+}$ are slightly smaller than a monomeric Chl $a^{\cdot+}$ (Deligiannakis and Rutherford, 2001). This is consistent with previous findings that the primary donor, P_{700}, comprised a strongly electronically coupled Chl a dimer (Norris et al., 1971; Webber and Lubitz, 2001), where the unpaired electron spin density distribution is asymmetric over the two Chl a molecules (3:1 or 4:1 ratio). The similar magnitude of the A_{iso} values of $A_0^{\cdot-}$ and $P_{700}^{\cdot+}$ indicates that the unpaired electron spin density is also delocalized over two or more Chl a rings in the $A_0^{\cdot-}$ state of PS I. Additionally, while the A_{iso} values range from 1.4–2.8 MHz for the nitrogen atoms of $P_{700}^{\cdot+}$, the corresponding A_{iso} values of 0.52–2.80 MHz in the $A_0^{\cdot-}$ state suggests a difference in the electron spin density distribution on the pyrrole nitrogen atoms, likely due to a change in the relative distance and orientation of the Chl molecules comprising A_0. While electron spin delocalization is apparent in the $A_0^{\cdot-}$ state, the 2D ^{14}N HYSCORE measurements do not identify the Chl molecules involved.

DFT confirms electron spin delocalization in the $A_0^{\cdot-}$ state

We performed DFT calculations to further understand the electron spin delocalization in the $A_0^{\cdot-}$ state. Typically, quantum mechanics/molecular modeling (QM/MM) methods have been used for computational studies of cofactors in redox proteins that include intensive quantum mechanical calculations on a small group of selected atoms, while classical treatment is used for the rest of the system (Kamerlin et al., 2009; Sproviero et al., 2006). The strong electronic coupling between the Chl rings in the primary donor Chl, $Chl_{1A/1B}$, and the close proximity of $Chl_{1A/1B}$, $Chl_{2A/2B}$, Chl_{3A}, and A_{1A} would likely complicate the use of hybrid methods. However, recent studies by Pantazis et al. (Sirohiwal et al., 2020) on highly coupled Chl and pheophytin molecules in photosystem II (PS II) suggests that future refinement of this system using QM/MM methods is possible. In the present study, we used an all-quantum mechanical approach to model the electronic structure of the cofactors as a whole (Charles et al., 2020). We derived the computational model from the X-ray crystal structure of cyanobacterial PS I (Jordan et al., 2001). Initially, we selected a simple monomeric Chl $a^{\cdot-}$ model, $Chl_{3A}^{\cdot-}$, as a starting point for the DFT calculations. The electron spin density distribution across the isolated $Chl_{3A/3B}^{\cdot-}$ anion (Figure S9) is in agreement with previously published literature on monomeric Chl $a^{\cdot-}$ in vitro (Parusel and Grimme, 2000; O'Malley, 2000a; Huber, 2001; Sinnecker et al., 2000). Interestingly, while the electron spin density has previously been observed to be uniformly distributed across the pyrrole nitrogen atoms in a Chl $a^{\cdot+}$ cation (O'Malley, 2000a; Sinnecker et al., 2002, O'Malley and Collins, 2001), we (and others) have observed that the distribution is asymmetric in a Chl $a^{\cdot-}$ anion (O'Malley, 2000a,b; Sinnecker et al., 2002).

To determine the effects of protein-cofactor interactions, we systematically expanded the computational model to include the $Met668_{PsaA}$ ligand of Chl_{3A}, a neighboring hydrogen-bonded residue, $Tyr696_{PsaA}$, the A_{1A} phylloquinone, the 'accessory' Chl, $Chl_{2A/2B}$, and the primary donor Chls, $Chl_{1A/1B}$. We discovered that, with the exception of A_{1A}, each additional cofactor that was included in the expanded computational models had a significant impact on the electron density distribution. When compared to the Chl $a^{\cdot-}$ anion, including the axial ligand, $Met668_{PsaA}$, and H-bonded residue, $Tyr696_{PsaA}$ of $Chl_{3A}^{\cdot-}$ saw a shift in the electron spin density distribution across the pyrrole nitrogens, whereby three nitrogens had a slight increase in electron density at the expense of the fourth nitrogen atom (Figure S10). Upon including the 'accessory Chl', Chl_{2A}, with its axial water ligand, and the A_{1A} cofactor (Figure 3A) or by considering a 'full chain model' with A_{1A}, Chl_{3A}, $Chl_{2A/2B}$, primary donor Chls, $Chl_{1A/1B}$ and their respective ligands (Figure S11), we observed asymmetric delocalization of electron spin density across both Chl_{3A} and Chl_{2A} in the singly occupied molecular orbital (SOMO) of the $A_0^{\cdot-}$ state. Interestingly, the only cofactor that did not demonstrate a discernable impact on charge delocalization in the $A_0^{\cdot-}$ state was the phylloquinone acceptor, A_{1A}. To facilitate a direct comparison of the spin delocalization, we also performed DFT calculations on the $P_{700}^{\cdot+}$ state of PS I using a computational model that contained Chl_{1A} and Chl_{1B} and their respective axial ligands (Jordan et al., 2001). Similar to previous studies, we observed that there is a distribution of the electron spin density on the $Chl_{1A/1B}$ molecules in the SOMO of the primary donor cation, $P_{700}^{\cdot+}$ (Figure 3B) (Plato et al., 2003), which is similar to the distribution in the $A_0^{\cdot-}$ state (Figure 3A) albeit to different extents. This indicates that both the primary donor and acceptor, $P_{700}^{\cdot+}$ and $A_0^{\cdot-}$, comprised a dimeric Chl motif with extensive electron spin delocalization. Comparison of Figures 3A and 3B indicates that the electron spin density is uniformly distributed across the pyrrole nitrogen atoms on each Chl ring in $P_{700}^{\cdot+}$ while it is asymmetric in the $A_0^{\cdot-}$ state. This is similar to earlier observations on Chl $a^{\cdot+}$ and Chl $a^{\cdot-}$ in vitro.

The electron spin density distribution in the SOMO that was observed in the DFT calculations (Figure 3A) corroborates the delocalization of the unpaired electron spin on at least three nitrogen atoms that were
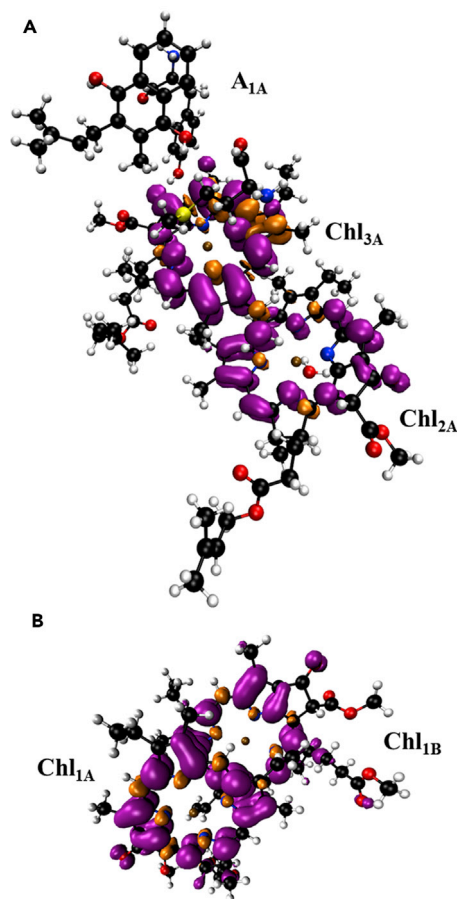
Figure 3. Electron spin density distribution in the singly occupied molecular orbital (SOMO) of the $A_0^{\cdot-}$ and $P_{700}^{\cdot+}$ state

Electron spin density distribution in the singly occupied molecular orbital (SOMO) of the (A) $A_0^{\cdot-}$ state in a computational model containing the A_{1A}, Chl_{3A} and Chl_{2A} cofactors as well as the $Met688_{PsaA}$ and $Tyr696_{PsaA}$ residues that are axially ligated and hydrogen bonded to Chl_{3A} cofactor, respectively, and the axial water ligand of the Chl_{2A} cofactor and (B) the $P_{700}^{\cdot+}$ state in a computational model containing the Chl_{1A} and Chl_{1B} cofactors and their respective axial ligands. The positive and negative spin densities are rendered in purple and yellow, respectively. The calculated hyperfine coupling constants and relative electron spin populations that are obtained from the DFT calculations of the computational model of the $A_0^{\cdot-}$ state (part (A)) are shown in Figures S12 and S13, respectively. For comparison, the electron-spin density distribution in the SOMO of an isolated $Chl_{3A}^{\cdot-}$ anion, $Chl_{3A}^{\cdot-}$ anion with the $Met688_{PsaA}$ and $Tyr696_{PsaA}$ residues and "full-chain" model with the A_{1A}, Chl_{3A}, $Chl_{2A/2B}$, $Chl_{1A/1B}$ cofactors and the $Met688_{PsaA}$ and $Tyr696_{PsaA}$ residues is shown in Figures S9–S11, respectively.

observed in the 2D ^{14}N HYSCORE spectroscopy measurements of the $A_0^{\cdot-}$ state (Tables 1 and S1). Moreover, a comparison of the experimental ^{14}N hyperfine coupling constants with the couplings that were calculated by DFT methods indicates that the hyperfine-coupled N^A and N^B nitrogen atoms in the 2D HYSCORE measurements correspond to the nitrogen atoms at the N^1 and N^2 of Chl_{3A} and N^C matches the N^2 and N^3 atoms of Chl_{2A} in the $A_0^{\cdot-}$ state (Figure S12 and Table S4). The DFT calculations predict hyperfine couplings of 1.3–1.4 MHz with the N^3 and N^1 atom on Chl_{3A} and Chl_{2A}, respectively. HYSCORE simulations using the calculated hyperfine and quadrupolar parameters that were obtained for the N^3 and N^1 atom on Chl_{3A} and Chl_{2A} suggest that the experimental cross-peaks should appear at frequencies close to those that arise from N^C. However, hyperfine signals from these nitrogen atoms were not detected in the 2D ^{14}N HYSCORE experiments. It is possible that the cross-peaks with hyperfine couplings of 1.3–1.4 MHz are overlapping and may be diminished in intensity due to cross-suppression effects from the hyperfine coupled N^1 and N^2 atoms of Chl_{3A} (Stoll et al., 2005; Taguchi et al., 2017). The resolution of the hyperfine signals of the N^3 and N^1 atoms on Chl_{3A} and Chl_{2A} will be the focus of future studies. In principle, it should

also be possible to resolve these nitrogens by using PS I isotopically labeled with ^{15}N, as was done with the primary donor in *Rhodobacter sphaeroides* (Lendzian et al., 1992, 1993). This would be a useful experiment to perform with the understanding, however, that such experiments would come at the loss of information on the quadrupolar coupling (Jarvis et al., 2019). The quantitative prediction of magnetic parameters using DFT methods that are described in this section neglect long-range interactions, such as those of the nearby Chl of the primary donor, P_{700}, which may influence the magnitude of the coupling constants. However, the agreement between the calculated and experimentally measured hyperfine and quadrupolar coupling constants (Figure S12 and Table S4) suggests that such effects may be limited in this system.

DISCUSSION

The most revealing features of the 2D HYSCORE spectroscopic measurements of the $A_0{}^{\cdot-}$ state are the isotropic hyperfine coupling constants, A_{iso}, that are related to the distribution of electron spin density on the constituent magnetically-active nitrogen atoms (Pandey and Chandra, 1979). The A_{iso} values of 0.52–2.80 MHz for $N^A - N^C$ indicate that the electron spin density is distributed on at least three distinct nitrogen atoms of $A_0{}^{\cdot-}$. Moreover, these A_{iso} values are less than those of a monomeric Chl $a^{\cdot+}$ cation (3.18–0.75) (Deligiannakis and Rutherford, 2001) or Chl $a^{\cdot-}$ anion (5.50–0.55) (Hoff et al., 1982) *in vitro*. The A_{iso} values are, however, similar in magnitude to the ^{14}N and ^{15}N hyperfine coupling constants (when scaled by the respective gyromagnetic ratios) for the strongly electronically coupled primary donor cation, $P_{700}{}^{\cdot+}$ and $P_{865}{}^{\cdot+}$, of PS I (Table S2) and the bacterial reaction center (bRC), respectively (Mac et al., 1998; Rigby et al., 2003; Webber and Lubitz, 2001; Käβ et al., 1995; Käβ and Lubitz, 1996; Kaess et al., 1995; Deligiannakis and Rutherford, 2001). These observations provide direct evidence that the unpaired electron spin in the $A_0{}^{\cdot-}$ state is delocalized over two (or more) Chl a molecules in PS I. Additionally, DFT calculations on an extended cofactor model in the A-branch of PS I unambiguously demonstrate that the electron spin density in the $A_0{}^{\cdot-}$ state is delocalized on the Chl_{2A} and Chl_{3A} molecules.

An important factor to consider in such a dimeric system is the extent of delocalization across the two cofactors. The Mulliken atomic spin populations on the nitrogen atoms, $N^1 - N^4$, of Chl_{3A} and Chl_{2A} that were obtained from the DFT calculations of the $A_0{}^{\cdot-}$ state allow us to estimate the delocalization of electron spin density across the two Chl rings (Figure S13). Interestingly, the distribution of the electron spin density over the dimer of Chl is asymmetric, where the electron spin delocalization on Chl_{3A} is favored by a factor of ~3.0. This is similar to other known dimeric Chl pairs, such as P_{700}, where previous DFT studies have suggested that while the SOMO of bare $P_{700}{}^{\cdot+}$ sees virtually identical spin density distribution across $Chl_{1A/1B}$ (Sun et al., 2006), the $P_{700}{}^{\cdot+}$ state within the native protein environment shows an asymmetry of the spin density distribution that arises from a hydrogen bond to one of the Chls in the dimer.

It is important to consider the possibility that the chemical treatment used to remove the phylloquinones (and antenna Chl) in wild-type PS I (see Method details section) could influence the primary charge separation reaction. However, inhibition of charge separation by such treatments is unlikely as previous studies using ether- (Ikegami et al., 1987) and ether/acetaldehyde-treated (Ikegami et al., 1995) PS I have demonstrated successful formation of the primary donor cation, $P_{700}{}^{\cdot+}$, upon illumination. Moreover, we observed that the loss of antenna Chls does not have an impact on the charge-separation reaction as the $\Delta menB$ variant of PS I with a mild detergent treatment (see STAR Methods) yields virtually identical spectral features in the $A_0{}^{\cdot-}$ state (Figure S5). The removal of the A_1 cofactor by chemical treatment and/or interruption of phylloquinone biosynthesis could result in small perturbations of the protein environment. However, a recent study where forward ET was halted without altering the A_1 binding pocket also yielded identical hyperfine interactions in the $A_0{}^{\cdot-}$ state and the spin density distribution of the $A_0{}^{\cdot-}$ state in the current DFT calculations is not impacted by the presence or absence of the phylloquinone cofactor, A_{1A} (Gorka et al., 2021). Therefore, while there are inherent uncertainties associated with the chemical or genetic modification of PS I, it is clear that changes to the phylloquinone binding pocket do not impact the electronic properties of the $A_0{}^{\cdot-}$ state.

Comparison of the relative orientation of Chl_{3A} and Chl_{2A} in the X-ray crystal structure of PS I (Jordan et al., 2001) reveals a close resemblance with the $Chl_{1A/1B}$ dimer in the primary donor, P_{700}. As can be seen in Figures 4A–4D, the ring planes of the Chl molecules in both cases are parallel to each other in a π-stacked orientation. The distance between the Chl_{3A} and Chl_{2A} ring in the direction perpendicular to the ring plane along the z axis is 3.9 Å (Figures 4A and 4B), which is nearly identical to the $Chl_{1A/1B}$ dimer of P_{700} (Figures 4C and 4D). The only substantive difference is the relative orientation of Chl_{2A} and Chl_{3A}, as there is a slight

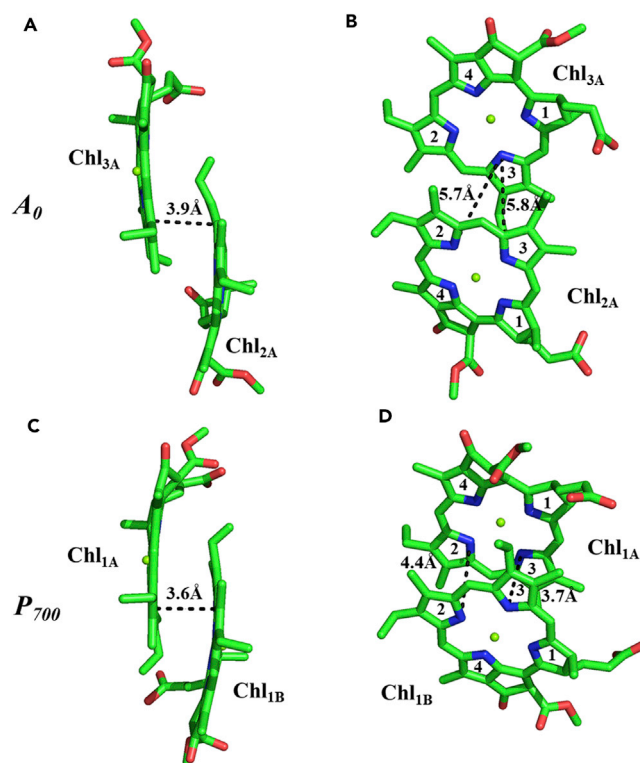**Figure 4. Structural comparison of the A_0 and P_{700} dimers in PS I**

Relative orientation and distances of the (A and B) Chl_{3A} and Chl_{2A} cofactors in the A_0 acceptor and (C and D) $Chl_{1A/1B}$ in the primary donor, $P_{700,}$ of cyanobacterial PS I (Jordan et al., 2001).

rotation in the ring plane which manifests as a change in the identity of the nearest pyrrole nitrogen atom in the neighboring ring. The N^3 nitrogen from Chl_{1A} in P_{700} is proximal to the N^3 nitrogen of Chl_{1B} (3.6 Å distance); however, the N^3 nitrogen of Chl_{3A} is nearly equidistant to the N^3 and N^2 nitrogens of Chl_{2A} (5.8 and 5.7 Å, respectively). This difference in the relative orientation of Chl_{2A} and Chl_{3A} in A_0 is best described as a "sliding" of the two Chl a rings away from each other along the X axis by ∼3 Å. This suggests that the coupling between the Chl_{3A} and Chl_{2A} rings of A_{0A} should be weaker than the coupling of $Chl_{1A/1B}$ in the primary donor, P_{700}.

It is important to note that while the DFT calculations were only performed on $A_0^{·−}$ in the A-branch, the distance and relative orientation of the analogous Chl cofactors of the B-branch, Chl_{2B} and Chl_{3B}, are similar. The distance between the nearest ring nitrogen atoms is 5.7 Å and 5.4 Å for the A- and B-branch, respectively, and both display a parallel orientation. There is a minor difference between the relative orientation of the Chl_{2A}/Chl_{3A} and Chl_{2B}/Chl_{3B} dimers, as the rotation in the X-Y plane is less extensive (relative to P_{700}) on the B-branch, resulting in the identity of the nearest nitrogen atom that more closely resembles P_{700}, i.e. the N^3 nitrogen of Chl_{2B} is close to the N^3 nitrogen of Chl_{3B}. Despite the subtle differences in the placement of Chl_{2B} and Chl_{3B}, we expect that the delocalization of the electron spin is similar in the $A_{0B}^{·−}$ state. It is currently unknown how much, if any, of the B-side is visible in our experiments and we plan on addressing the nature of the B-side ET in future studies.

The significant electron spin delocalization over the $Chl_{2A/2B}$ and $Chl_{3A/3B}$ cofactors in the $A_0^{·−}$ state provides unique insights into the previously unknown role of the "accessory chlorophylls", $Chl_{2A/2B}$, of PS I. Our results clearly indicate that it is important to consider $Chl_{2A/2B}$ and $Chl_{3A/3B}$ in the $A_{0A/0B}^{·−}$ state in the same light as the electronically coupled $Chl_{1A/1B}$ dimer in the primary donor cation, $P_{700}^{·+}$ (Madjet et al., 2009). The presence of an electronically coupled dimeric Chl motif has a pronounced influence on the nature of the electron donor and acceptors of PS I. ET between a given donor (D) and acceptor (A) in a RC was previously considered a discrete event where the kinetics are governed by factors such as

the inter-cofactor distance, free energy difference, protein motion, and dielectric environment (Moser et al., 1992; Moia et al., 2020). However, based on our findings and those of others (Cherepanov et al., 2021) the initial light-driven charge separation in type I RCs may not be a discrete event that can be described by a simple D-A system. Instead, there is extended delocalization of electron density across a set of multiple coupled cofactors, or an exciplex, that is driven by downhill energetics. This provides a spatial separation of charges that occurs faster than de-excitation of the photo-excited primary donor, P_{700}^*, alone. Previous calculations have suggested a process whereby the coupling of $Chl_{2A/2B}$ and $Chl_{3A/3B}$ may be the key to lowering the redox potential of the A_0 electron acceptor so as to ensure that the formation of the charge-separated state is energetically favorable (Ptushenko et al., 2008). However, experimental evidence for such a coupling was lacking to date. It is important to note that the A_{1A} cofactor (located 6.7 Å from Chl_{3A}) does not have a discernable effect on the electron spin density distribution over the Chl_{2A} and Chl_{3A} rings individually or collectively, suggesting that the ET reactions after primary charge separation occur in a discrete fashion.

Efficient charge separation is not the sole requirement for attaining high quantum efficiency in RCs. To compete effectively with charge recombination, charge separation must be accompanied by rapid multi-step forward ET through one or more electron acceptors. The spatial separation afforded by the dimeric Chl motif of $A_0^{\cdot-}$, as opposed to a Chl monomer located closer to P_{700}, likely prevents ultrafast charge recombination with $P_{700}^{\cdot+}$ thus allowing for forward ET to the A_1 cofactor (Figure 1B). This is an important principle that could be incorporated in the design of artificial photosynthetic RCs that currently suffer from relatively low quantum yields and rapid charge recombination reactions (Llansola-Portoles et al., 2017). The incorporation of highly coupled donors and acceptors would allow for extensive delocalization that could prolong the lifetime of the charge-separated state with high quantum efficiency over a wide range of excitation wavelengths.

Photosynthetic RCs in a wide variety of organisms employ two symmetric branches of cofactors for light-driven charge separation and ET (Lancaster et al., 2007; Roy et al., 1995; Jordan et al., 2001; Umena et al., 2011; Gisriel et al., 2017) where, in addition to a primary donor (B)Chl, each branch also contains an accessory (B)Chl molecule. In light of our evidence for direct charge delocalization in the $A_0^{\cdot-}$ state of PS I, it is worth examining the nature and evolution of primary charge separation in other photosynthetic RCs. The homodimeric heliobacterial reaction center (HbRC) is considered to be the exemplar of ancestral PS I due to its structural and functional simplicity (Sattley and Swingley, 2013; Cardona, 2015; Ferlez et al., 2016; Orf et al., 2018). The ET pathway of the HbRC only contains two electron acceptors, namely, A_0 and a single [4Fe–4S] cluster, F_X (Ferlez et al., 2016; Gisriel et al., 2017). Similar to PS I, the core of the HbRC contains an "accessory" Chl molecule, $BChl_{2A}$, which is positioned between $BChl_{1A}$ and Chl_{3A} (where "B" refers to "bacterio"). It is interesting that the 8^1-OH Chl a and BChl g molecules of the HbRC are nearly identical in orientation to the analogous cofactors in PS I (Figures 5A and 5B), where the center-to-center distance between the two rings is 3.4 Å, but with a longer distance of ∼6.3 Å to the nearest nitrogen atom. This is in stark contrast to type II RCs (the bRC and PS II), where the relative orientation of the Chl_{2A} and Chl_{3A} pair deviates significantly from a parallel orientation (Figures 5C and 5D) and the chemical identity of the Chl_{3A} acceptor is a (B)pheophytin ((B)Pheo) of the (B)Chl of the primary donor, while all known type I RCs contain a Chl a (or close derivative) in this site (Orf et al., 2018; Chen et al., 2020).

The differences in type I and type II RCs in terms of their primary acceptors likely reflects different strategies to control primary charge separation. It is important that charge separation in the RC take place rapidly and prior to de-excitation of the primary donor, which would require sufficiently downhill energy transfer. In the case of Type II RCs, a driving force of approximately 300 mV is gained by introducing (B)Pheo instead of (B)Chl as the primary acceptor (Fajer et al., 1975). Recent studies on PS II suggest that this gap is widened by protein-matrix effects, which redshifts the primary donor (suggested to be Chl_{2A}) and blue shifts the primary acceptor (Sirohiwal et al., 2020). This is reflected in the findings of both pulsed EPR measurements and theoretical calculations on the reduced (B)Pheo$^{\cdot-}$ state. The A_{iso} values for both monomeric Pheo$^{\cdot-}$ in $vitro$ (Lendzian et al., 1982) and photoaccumulated Pheo$^{\cdot-}$ in PS II (Deligiannakis and Rutherford, 1997) that were determined through ^{14}N ENDOR and ESEEM, respectively, are shown in Table 1. The A_{iso} values of for both Pheo$^{\cdot-}$ (O'Malley, 2000b) and (B)Pheo$^{\cdot-}$ (O'Malley, 1999) in conjunction with large scale calculations on the early acceptors in PS II (Sirohiwal et al., 2020) provide unambiguous evidence that the electron spin density on the primary acceptor (A_0) of Type II RCs is localized entirely on the (B) Pheo cofactor. This is noteworthy as it indicates that: (1) electron delocalization across the primary acceptor
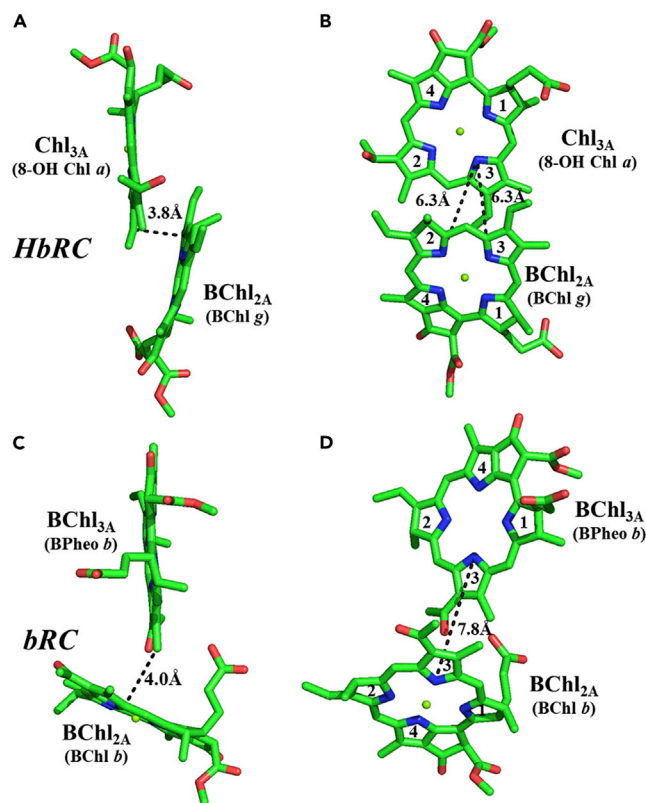
Figure 5. Structural comparison of primary acceptor motifs in other type I and type II RCs
Relative orientation and distances of the (B)Chl$_{3A}$ and (B)Chl$_{2A}$ cofactors in the primary acceptor positions for the (A and B) heliobacterial reaction center (Gisriel et al., 2017) and (C and D) purple bacterial reaction center (Lancaster et al., 2007).

with a dimeric Chl motif is not required for highly efficient energy transfer in these RCs, and (2) both type I and type II RCs utilize extensive protein-cofactor interactions (Srinivasan and Golbeck, 2009; Sirohiwal et al., 2020) to tune the energetic and electronic properties of its cofactors, albeit to different ends.

In contrast, type I RCs do not have the luxury of an inherent loss of free energy, as they are fixed with a Chl a as the primary acceptor, regardless of the identity of the primary donor. The reason for fixing Chl a as the acceptor is not fully understood; but regardless, Type I RCs must deal with the energetic restrictions of that Chl. To cope with this restriction, type I RCs evolved different methods to tune the energetics of their redox cofactors so as to ensure that both charge separation is favored and subsequent charge recombination is inhibited in varying landscapes of possible acceptors. For example, one major difference between the HbRC and PS I is the addition of a bound quinone (A$_1$) in the acceptor chain in PS I, which is thought to prevent triplet state formation when recombining from Chl$_{3A}$·$^-$, albeit at the expense of marginally slower forward ET (reviewed in (Orf et al., 2018)). In PS I, A$_0$ and A$_1$ are poised at redox potentials sufficient to allow forward ET from A$_0$·$^-$ to A$_1$ and then from A$_1$·$^-$ to F$_X$, all while preventing recombination from these cofactors, not a trivial task when the identity of the Chl$_3$ is fixed. However, not only has Chl dimerization been shown to have an impact on the redox potential (Ptushenko et al., 2008), but the coupling between monomers is tunable by altering the distance between the π-planes (Madjet et al., 2009). Thus, the employment of a dimeric motif to control the nature and extent of delocalization became a tool that nature used to precisely tune the energetics of the ET cofactors, and in this case, the efficiency of charge separation itself.

Limitations of the study
There are limitations of this study that should be considered when extending the model to other systems. For application of our model to other type I and type II RCs, it is important to consider that there can be significant variations in the electronic structure and protein-matrix influences of a certain cofactor in the

same protein but from different species. Therefore, specific RCs would need tested before we can have a high confidence in the broad applicability of our model.

STAR★METHODS

Detailed methods are provided in the online version of this paper and include the following:

- KEY RESOURCES TABLE
- RESOURCE AVAILABILITY
  - Lead contact
  - Materials availability
  - Data availability
- METHOD DETAILS
  - Preparation of photosystem I samples
  - Trapping of the $A_{0A}^{\cdot-}$ state
  - Pulsed electron paramagnetic resonance spectroscopy
  - DFT calculations

SUPPLEMENTAL INFORMATION

Supplemental information can be found online at https://doi.org/10.1016/j.isci.2021.102719.

A video abstract is available at https://doi.org/10.1016/j.isci.2021.102719#mmc2.

AUTHOR CONTRIBUTIONS

M.G., P.C., V.K., and A.B. conducted experiments, analyzed the data, and performed calculations; M.G., K.V.L., and J.H.G. designed the experiments and wrote the paper.

DECLARATION OF INTERESTS

The authors declare no competing interests.

INCLUSION AND DIVERSITY

While citing references scientifically relevant for this work, we also actively worked to promote gender balance in our reference list.

REFERENCES

Anderson, J.M. (1982). The role of chlorophyll-protein complexes in the function and structure of chloroplast thylakoids. Mol. Cell Biochem. 46, 161–172.

Ayers, P.W. (2005). An elementary derivation of the hard/soft-acid/base principle. J. Chem. Phys. 122, 141102.

Brettel, K., and Leibl, W. (2001). Electron transfer in photosystem I. Biochim. Biophys. Acta Bioenerg. 1507, 100–114.

Britt, R.D., Campbell, K.A., Peloquin, J.M., Gilchrist, M.L., Aznar, C.P., Dicus, M.M., Robblee, J., and Messinger, J. (2004). Recent pulsed EPR studies of the photosystem II oxygen-evolving complex: Implications as to water oxidation mechanisms. Biochim. Biophys. Acta Bioenerg. 1655, 158–171.

Cardona, T. (2015). A fresh look at the evolution and diversification of photochemical reaction centers. Photosynth Res. 126, 111–134.

Charles, P., Kalendra, V., He, Z., Khatami, M.H., Golbeck, J.H., van der Est, A., Lakshmi, K.V., and Bryant, D.A. (2020). Two-dimensional ^{67}Zn HYSCORE spectroscopy reveals that a Zn-bacteriochlorophyll $a_P{}'$ dimer is the primary donor (P$_{840}$) in the type-1 reaction centers of *Chloracidobacterium thermophilum*. Phys. Chem. Chem. Phys. 22, 6457–6467.

Chatterjee, R., Milikisiyants, S., Coates, C.S., and Lakshmi, K.V. (2011). High-resolution two-dimensional ^{1}H and ^{14}N hyperfine sublevel

correlation spectroscopy of the primary quinone of photosystem II. Biochemistry 50, 491–501.

Chauvet, A., Dashdorj, N., Golbeck, J.H., Johnson, T.W., and Savikhin, S. (2012). Spectral resolution of the primary electron acceptor A_0 in photosystem I. J. Phys. Chem. B 116, 3380–3386.

Chen, J.-H., Wu, H., Xu, C., Liu, X.-C., Huang, Z., Chang, S., Wang, W., Han, G., Kuang, T., Shen, J.-R., and Zhang, X. (2020). Architecture of the photosynthetic complex from a green sulfur bacterium. Science 370, eabb6350.

Cherepanov, D.A., Shelaev, I.V., Gostev, F.E., Aybush, A.V., Mamedov, M.D., Shuvalov, V.A., Semenov, A.Y., and Nadtochenko, V.A. (2020). Generation of ion-radical chlorophyll states in the light-harvesting antenna and the reaction center of cyanobacterial photosystem I. Photosyn Res. 146, 55–73.

Cherepanov, D.A., Shelaev, I.V., Gostev, F.E., Petrova, A., Aybush, A.V., Nadtochenko, V.A., Xu, W., Golbeck, J.H., and Semenov, A.Y. (2021). Primary charge separation within the structurally symmetric tetrameric $Chl_{2A}P_AP_BChl_{2B}$ chlorophyll exciplex in photosystem I. J. Photochem. Photobiol. B 217, 112154.

Cohen, R.O., Shen, G., Golbeck, J.H., Xu, W., Chitnis, P.R., Valieva, A.I., van der Est, A., Pushkar, Y., and Stehlik, D. (2004). Evidence for asymmetric electron transfer in cyanobacterial photosystem I: Analysis of a methionine-to-leucine mutation of the ligand to the primary electron acceptor A_0. Biochemistry 43, 4741–4754.

Commoner, B., Heise, J.J., and Townsend, J. (1956). Light-induced paramagnetism in chloroplasts. Proc. Natl. Acad. Sci. U S A. 42, 710–718.

Dashdorj, N., Xu, W., Cohen, R.O., Golbeck, J.H., and Savikhin, S. (2005). Asymmetric electron transfer in cyanobacterial photosystem I: Charge separation and secondary electron transfer dynamics of mutations near the primary electron acceptor A_0. Biophys. J. 88, 1238–1249.

Davis, I.H., Heathcote, P., Maclachlan, D.J., and Evans, M.C.W. (1993). Modulation analysis of the electron spin echo signals of in vivo oxidised primary donor ^{14}N chlorophyll centres in bacterial, P_{870} and P_{960}, and plant photosystem I, P_{700}, reaction centres. Biochim. Biophys. Acta Bioenerg. 1143, 183–189.

Deligiannakis, Y., Hanley, J., and Rutherford, A.W. (1998). Spin-lattice relaxation of the phyllosemiquinone radical of photosystem I. Biochemistry 37, 3329–3336.

Deligiannakis, Y., Hanley, J., and Rutherford, A.W. (1999). 1D- and 2D-ESEEM study of the semiquinone radical Q_A^{-} of photosystem II. J. Amer Chem Soc. 121, 7653–7664.

Deligiannakis, Y., Louloudi, M., and Hadjiliadis, N. (2000). Electron spin echo envelope modulation (ESEEM) spectroscopy as a tool to investigate the coordination environment of metal centers. J. Coord. Chem. 204, 1–112.

Deligiannakis, Y., and Rutherford, A.W. (1997). One- and two-dimensional electron spin echo envelope modulation study of the intermediate electron acceptor pheophytin in ^{14}N- and ^{15}N-

labeled photosystem II. J. Amer Chem. Soc. 119, 4471–4480.

Deligiannakis, Y., and Rutherford, A.W. (2001). Electron spin echo envelope modulation spectroscopy in photosystem I. Biochim. Biophys. Acta Bioenerg. 1507, 226–246.

Fajer, J., Brune, D.C., Davis, M.S., Forman, A., and Spaulding, L.D. (1975). Primary charge separation in bacterial photosynthesis: Oxidized chlorophylls and reduced pheophytin. Proc. Natl. Acad. Sci. U S A 72, 4956–4960.

Fajer, J., Davis, M.S., Forman, A., Klimov, V.V., Dolan, E., and Ke, B. (1980). Primary electron acceptors in plant photosynthesis. J. Amer. Chem. Soc. 102, 7143–7145.

Ferlez, B., Cowgill, J., Dong, W., Gisriel, C., Lin, S., Flores, M., Walters, K., Cetnar, D., Redding, K.E., and Golbeck, J.H. (2016). Thermodynamics of the electron acceptors in Heliobacterium modesticaldum: An exemplar of an early homodimeric Type I photosynthetic reaction center. Biochemistry 55, 2358–2370.

Forman, A., Davis, M.S., Fujita, I., Hanson, L.K., Smith, K.M., and Fajer, J. (1981). Mechanisms of energy transduction in plant photosynthesis: ESR, ENDOR and MOs of the primary acceptors. Isr. J. Chem. 21, 265–269.

Fromme, P., Jordan, P., and Kraus, N. (2001). Structure of photosystem I. Biochim. Biophys. Acta Bioenerg. 1507, 5–31.

García-Rubio, I., Martínez, J.I., Picorel, R., Yruela, I., and Alonso, P.J. (2003). HYSCORE spectroscopy in the cytochrome b_{559} of the photosystem II reaction center. J. Amer. Chem. Soc. 125, 15846–15854.

Gibasiewicz, K., Ramesh, V.M., Lin, S., Redding, K., Woodbury, N.W., and Webber, A.N. (2003). Excitonic interactions in wild-type and mutant PSI reaction centers. Biophys. J. 85, 2547–2559.

Gisriel, C., Sarrou, I., Ferlez, B., Golbeck, J.H., Redding, K.E., and Fromme, R. (2017). Structure of a symmetric photosynthetic reaction center-photosystem. Science 357, 1021–1025.

Golbeck, J.H. (2006). Photosystem I: The Light-Driven Plastocyanin: Ferredoxin Oxidoreductase (Springer).

Gorka, M., Gruszecki, E., Charles, P., Kalendra, V., Lakshmi, K.V., and Golbeck, J.H. (2021). Two-dimensional HYSCORE spectroscopy reveals a histidine imidazole as the axial ligand to Chl_{3A} in the $M688H_{PsaA}$ genetic variant of Photosystem I. Biochim. Biophys. Acta Bioenerg. 1862, 148424.

Harmer, J., Mitrikas, G., and Schweiger, A. (2009). Advanced pulse EPR methods for the characterization of metalloproteins. In High Resolution EPR: Applications to Metalloenzymes and Metals in Medicine, L. Berliner and G. Hanson, eds. (Springer), pp. 13–61.

Höfer, P., Grupp, A., Nebenführ, H., and Mehring, M. (1986). Hyperfine sublevel correlation (HYSCORE) spectroscopy: A 2D ESR investigation of the squaric acid radical. Chem. Phys. Lett. 132, 279–282.

Hoff, A.J., Lendzian, F., Möbius, K., and Lubitz, W. (1982). Proton and nitrogen electron nuclear

double and triple resonance of the chlorophyll a anion in liquid solution. Chem. Phys. Lett. 85, 3–8.

Holzwarth, A.R., Müller, M.G., Niklas, J., and Lubitz, W. (2006). Ultrafast transient absorption studies on photosystem I reaction centers from Chlamydomonas reinhardtii. 2: Mutations near the P_{700} reaction center chlorophylls provide new insight into the nature of the primary electron donor. Biophys. J. 90, 552–565.

Huber, M. (2001). The role of the electronic structure of the porphyrin as viewed by EPR/ENDOR methods in the efficiency of biomimetic model compounds for photosynthesis. Eur. J. Org. Chem. 2001, 4379–4389.

Ikegami, I., Itoh, S., and Iwaki, M. (1995). Photoactive photosystem I particles with a molar ratio of chlorophyll a to P_{700} of 9. Plant Cell Physiol. 36, 857–864.

Ikegami, I., Itoh, S., and Iwaki, M. (2000). Selective extraction of antenna chlorophylls, carotenoids and quinones from photosystem I reaction center. Plant Cell Physiol. 41, 1085–1095.

Ikegami, I., and Kato, S. (1975). Enrichment of photosystem I reaction center chlorophyll from spinach chloroplasts. Biochim. Biophys. Acta 376, 588–592.

Ikegami, I., Sétif, P., and Mathis, P. (1987). Absorption studies of photosystem I photochemistry in the absence of vitamin K-1. Biochim. Biophys. Acta Bioenerg. 894, 414–422.

Ishikita, H., and Knapp, E.W. (2003). Redox potential of quinones in both electron transfer branches of photosystem I. J. Biol. Chem. 278, 52002–52011.

Itoh, S., Iwaki, M., and Ikegami, I. (1987). Extraction of vitamin K-1 from photosystem I particles by treatment with diethyl ether and its effects on the A_{-1} EPR signal and system I photochemistry. Biochim. Biophys. Acta Bioenerg. 893, 508–516.

Itoh, S., Iwaki, M., and Ikegami, I. (2001). Modification of photosystem I reaction center by the extraction and exchange of chlorophylls and quinones. Biochim. Biophys. Acta Bioenerg. 1507, 115–138.

Jarvis, J.A., Concistre, M., Haies, I.M., Bounds, R.W., Kuprov, I., Carravetta, M., and Williamson, P.T.F. (2019). Quantitative analysis of ^{14}N quadrupolar coupling using ^{1}H detected ^{14}N solid-state NMR. Phys. Chem. Chem. Phys. 21, 5941–5949.

Johnson, T.W., Shen, G., Zybailov, B., Kolling, D., Reategui, R., Beauparlant, S., Vassiliev, I.R., Bryant, D.A., Jones, A.D., Golbeck, J.H., and Chitnis, P.R. (2000). Recruitment of a foreign quinone into the A_1 site of photosystem I. I. Genetic and physiological characterization of phylloquinone biosynthetic pathway mutants in Synechocystis sp. pcc 6803. J. Biol. Chem. 275, 8523–8530.

Johnson, T.W., Zybailov, B., Jones, A.D., Bittl, R., Zech, S., Stehlik, D., Golbeck, J.H., and Chitnis, P.R. (2001). Recruitment of a foreign quinone into the A_1 site of photosystem I. J. Biol. Chem. 276, 39512–39521.

Jordan, P., Fromme, P., Witt, H.T., Klukas, O., Saenger, W., and Krauss, N. (2001). Three-dimensional structure of cyanobacterial photosystem I at 2.5 A resolution. Nature *411*, 909–917.

Kaess, H., Rautter, J., Boenigk, B., Hoefer, P., and Lubitz, W. (1995). 2D ESEEM of the ^{15}N-labeled radical cations of bacteriochlorophyll a and of the primary donor in reaction centers of *Rhodobacter sphaeroides*. J. Phys. Chem. *99*, 436–448.

Kamerlin, S.C.L., Haranczyk, M., and Warshel, A. (2009). Progress in *ab initio* QM/MM free-energy simulations of electrostatic energies in proteins: Accelerated QM/MM studies of pKa, redox reactions and solvation free energies. J. Phys. Chem. B *113*, 1253–1272.

Käss, H., Fromme, P., Witt, H.T., and Lubitz, W. (2001). Orientation and electronic structure of the primary donor radical cation in photosystem I: A single crystals EPR and ENDOR Study. J. Phys. Chem. B *105*, 1225–1239.

Katz, J.J., Norris, J.R., Shipman, L.L., Thurnauer, M.C., and Wasielewski, M.R. (1978). Chlorophyll function in the photosynthetic reaction center. Annu. Rev. Biophys. Bioeng. *7*, 393–434.

Käß, H., Bittersmann-Weidlich, E., Andréasson, L.E., Bönigk, B., and Lubitz, W. (1995). ENDOR and ESEEM of the ^{15}N labelled radical cations of chlorophyll a and the primary donor P_{700} in photosystem I. Chem. Phys. *194*, 419–432.

Käß, H., Fromme, P., and Lubitz, W. (1996). Quadrupole parameters of nitrogen nuclei in the cation radical $P_{700}^{\cdot+}$ determined by ESEEM of single crystals of photosystem I. Chem. Phys. Lett. *257*, 197–206.

Käß, H., and Lubitz, W. (1996). Evaluation of 2D ESEEM data of ^{15}N-labeled radical cations of the primary donor P_{700} in photosystem I and chlorophyll *a*. Chem. Phys. Lett. *251*, 193–203.

Kurashov, V., Gorka, M., Milanovsky, G.E., Johnson, T.W., Cherepanov, D.A., Semenov, A.Y., and Golbeck, J.H. (2018). Critical evaluation of electron transfer kinetics in P_{700}-F_A/F_B, P_{700}-F_X, and P_{700}-A_1 photosystem I core complexes in liquid and in trehalose glass. Biochim. Biophys. Acta Bioenerg. *1859*, 1288–1301.

Lakshmi, K.V., Jung, Y.-S., Golbeck, J.H., and Brudvig, G.W. (1999). Location of the iron−sulfur clusters F_A and F_B in photosystem I: An electron paramagnetic resonance study of spin relaxation enhancement of P_{700}^+. Biochemistry *38*, 13210–13215.

Lancaster, C.R., Hunte, C., Kelley, J., 3rd, Trumpower, B.L., and Ditchfield, R. (2007). A comparison of stigmatellin conformations, free and bound to the photosynthetic reaction center and the cytochrome bc$_1$ complex. J. Mol. Biol. *368*, 197–208.

Lendzian, F., Geßern, C., Bönigk, B., Plato, M., Möbius, K., and Lubitz, W. (1992). [15]N- and [1]H-ENDOR/TRIPLE resonance of the primary donor cation radical D$^{+\bullet}$ in isotopically labelled reaction centers of *Rhodobacter sphaeroides*. In Research in Photosynthesis, Proceedings of the IXth International Congress on Photosynthesis, N. Murata, ed. (Kluwer), pp. 57–68.

Lendzian, F., Huber, M., Isaacson, R.A., Endeward, B., Plato, M., Bönigk, B., Möbius, K., Lubitz, W., and Feher, G. (1993). The electronic structure of the primary donor cation radical in *Rhodobacter sphaeroides* R-26: ENDOR and TRIPLE resonance studies in single crystals of reaction centers. Biochim. Biophys. Acta Bioenerg. *1183*, 139–160.

Lendzian, F., Mobius, K., and Lubitz, W. (1982). The pheophytin a anion radical. [14]N and ^{1}H ENDOR and triple resonance in liquid solution. Chem. Phys. Lett. *90*, 375–381.

Li, Y., Est, A., Lucas, M., Vm, R., Gu, F., Petrenko, A., Lin, S., Webber, A., Rappaport, F., and Redding, K. (2006). Directing electron transfer within photosystem I by breaking H-bonds in the cofactor branches. Proc. Natl. Acad. Sci. U S A. *103*, 2144–2149.

Llansola-Portoles, M.J., Gust, D., Moore, T.A., and Moore, A.L. (2017). Artificial photosynthetic antennas and reaction centers. Comptes Rendus Chim. *20*, 296–313.

Lubitz, W., Lendzian, F., and Bittl, R. (2002). Radicals, radical pairs and triplet states in photosynthesis. Acc. Chem. Res. *35*, 313–320.

Mac, M., Bowlby, N.R., Babcock, G.T., and McCracken, J. (1998). Monomeric spin density distribution in the primary donor of photosystem I as determined by electron magnetic resonance: Functional and thermodynamic implications. J. Amer Chem. Soc. *120*, 13215–13223.

Mac, M., Tang, X.-S., Diner, B.A., McCracken, J., and Babcock, G.T. (1996). Identification of histidine as an axial ligand to P^{700+}. Biochemistry *35*, 13288–13293.

Madjet, M.E.-A., Müh, F., and Renger, T. (2009). Deciphering the influence of short-range electronic couplings on optical properties of molecular dimers: application to "special pairs" in photosynthesis. J. Phys. Chem. B *113*, 12603–12614.

Meyer, T.E. (1994). Evolution of photosynthetic reaction centers and light harvesting chlorophyll proteins. Biosystems *33*, 167–175.

Milanovsky, G.E., Ptushenko, V.V., Cherepanov, D.A., and Semenov, A.-Y. (2014). Mechanism of primary and secondary ion-radical pair formation in photosystem I complexes. Biochemistry *79*, 221–226.

Moia, D., Abe, M., Wagner, P., Saguchi, H., Koumura, N., Nelson, J., Barnes, P.R.F., and Mori, S. (2020). The effect of the dielectric environment on electron transfer reactions at the interfaces of molecular sensitized semiconductors in electrolytes. J. Phys. Chem. C *124*, 6979–6992.

Moser, C.C., Keske, J.M., Warncke, K., Farid, R.S., and Dutton, P.L. (1992). Nature of biological electron transfer. Nature *355*, 796–802.

Müller, M.G., Niklas, J., Lubitz, W., and Holzwarth, A.R. (2003). Ultrafast transient absorption studies on photosystem I reaction centers from *Chlamydomonas reinhardtii*. 1. A new interpretation of the energy trapping and early electron transfer steps in photosystem I. Biophys. J. *85*, 3899–3922.

Müller, M.G., Slavov, C., Luthra, R., Redding, K.E., and Holzwarth, A.R. (2010). Independent initiation of primary electron transfer in the two branches of the photosystem I reaction center. Proc. Natl. Acad. Sci. U S A. *107*, 4123–4128.

Neese, F. (2012). The ORCA program system. Wires Comput. Mol. Sci. *2*, 73–78.

Neese, F. (2018). Software update: the ORCA program system, version 4.0. Wires Comput. Mol. Sci. *8*, e1327.

Norris, J.R., Scheer, H., Druyan, M.E., and Katz, J.J. (1974). An electron-nuclear double resonance (ENDOR) study of the special pair model for photo-reactive chlorophyll in photosynthesis. Proc. Natl. Acad. Sci. U S A. *71*, 4897–4900.

Norris, J.R., Uphaus, R.A., Crespi, H.L., and Katz, J.J. (1971). Electron spin resonance of chlorophyll and the origin of signal I in photosynthesis. Proc. Natl. Acad. Sci. U S A. *68*, 625–628.

O'Malley, P.J. (1999). The electronic structure of the bacteriopheophytin a anion radical, *in vivo*. J. Amer. Chem. Soc. *121*, 3185–3192.

O'Malley, P.J. (2000a). The effect of oxidation and reduction of chlorophyll a on its geometry, vibrational and spin density properties as revealed by hybrid density functional methods. J. Amer Chem. Soc. *122*, 7798–7801.

O'Malley, P.J. (2000b). Hybrid density functional studies of pheophytin anion radicals: Implications for initial electron transfer in photosynthetic reaction centers. J. Phys. Chem. B *104*, 2176–2182.

Olson, J.M., and Pierson, B.K. (1987). Origin and evolution of photosynthetic reaction centers. Orig Life Evol. Biosph. *17*, 419–430.

O'Malley, P.J., and Collins, S.J. (2001). The effect of axial Mg ligation on the geometry and spin density distribution of chlorophyll and bacteriochlorophyll cation free radical models: A density functional study. J. Amer. Chem. Soc. *123*, 11042–11046.

Orf, G.S., Gisriel, C., and Redding, K.E. (2018). Evolution of photosynthetic reaction centers: insights from the structure of the heliobacterial reaction center. Photosynth. Res. *138*, 11–37.

Pandey, P.K.K., and Chandra, P. (1979). Theoretical study of isotropic hyperfine coupling constants in small radicals by MINDO/3 method. Can. J. Chem. *57*, 3126–3134.

Parusel, A.B.J., and Grimme, S. (2000). A theoretical study of the excited states of chlorophyll a and pheophytin a. J. Phys. Chem. B *104*, 5395–5398.

Pearson, R.G. (1963). Hard and soft acids and bases. J. Amer. Chem. Soc. *85*, 3533–3539.

Plato, M., Kraus, N., Fromme, P., and Lubitz, W. (2003). Molecular orbital study of the primary electron donor P_{700} of photosystem I based on a recent X-ray single crystal structure analysis. Chem. Phys. *294*, 483–499.

Poluektov, O.G., Paschenko, S.V., Utschig, L.M., Lakshmi, K.V., and Thurnauer, M.C. (2005). Bidirectional electron transfer in photosystem I: Direct evidence from high-frequency time-

resolved EPR spectroscopy. J. Amer. Chem. Soc. *127*, 11910–11911.

Ptushenko, V.V., Cherepanov, D.A., Krishtalik, L.I., and Semenov, A.Y. (2008). Semi-continuum electrostatic calculations of redox potentials in photosystem I. Photosyn Res. *97*, 55.

Rabinowitch, E.I., and Govindjee. (1965). The role of chlorophyll in photosynthesis. Sci. Amer. *213*, 74–83.

Rigby, S.E.J., Muhiuddin, I.P., Santabarbara, S., Evans, M.C.W., and Heathcote, P. (2003). Proton ENDOR spectroscopy of the anion radicals of the chlorophyll primary electron acceptors in type I photosynthetic reaction centres. Chem. Phys. *294*, 319–328.

Rögner, M., Nixon, P.J., and Diner, B.A. (1990). Purification and characterization of photosystem I and photosystem II core complexes from wild-type and phycocyanin-deficient strains of the cyanobacterium *Synechocystis* PCC 6803. J. Biol. Chem. *265*, 6189–6196.

Roy, C., Lancaster, D., Ermler, U., and Michel, H. (1995). The structures of photosynthetic reaction centers from purple bacteria as revealed by X-ray crystallography. In Anoxygenic Photosynthetic Bacteria, R.E. Blankenship, M.T. Madigan, and C.E. Bauer, eds. (Springer), pp. 503–526.

Sattley, W.M., and Swingley, W.D. (2013). Properties and evolutionary implications of the heliobacterial genome. Adv. Bot. Res. *66*, 67–97.

Savitsky, A., Gopta, O., Mamedov, M., Golbeck, J.H., Tikhonov, A., Möbius, K., and Semenov, A. (2009). Alteration of the axial met ligand to electron acceptor A_0 in photosystem I: effect on the generation of $P_{700}^{\cdot+}A_1^{\cdot-}$ radical pairs as studied by W-band transient EPR. Appl. Magn. Reson. *37*, 85.

Schnegg, A., Dubinskii, A.A., Fuchs, M.R., Grishin, Y.A., Kirilina, E.P., Lubitz, W., Plato, M., Savitsky, A., and Möbius, K. (2007). High-field EPR, ENDOR and ELDOR on bacterial photosynthetic reaction centers. Appl. Magn. Reson. *31*, 59–98.

Şener, M., Strümpfer, J., Hsin, J., Chandler, D., Scheuring, S., Hunter, C.N., and Schulten, K. (2011). Förster energy transfer theory as reflected in the structures of photosynthetic light-harvesting systems. Chem. Phys. Chem. *12*, 518–531.

Shelaev, I.V., Gostev, F.E., Mamedov, M.D., Sarkisov, O.M., Nadtochenko, V.A., Shuvalov, V.A., and Semenov, A.Y. (2010). Femtosecond primary charge separation in *Synechocystis* sp. PCC 6803 photosystem I. Biochim. Biophys. Acta *1797*, 1410–1420.

Shuvalov, V.A., Dolan, E., and Ke, B. (1979a). Spectral and kinetic evidence for two early electron acceptors in photosystem I. Proc. Natl. Acad. Sci. U S A. *76*, 770–773.

Shuvalov, V.A., Bacon, K.E., and Dolan, E. (1979b). Kinetic and spectral properties of the intermediary electron acceptor A_1 in photosystem I: Subnanosecond spectroscopy. FEBS Lett. *100*, 5–8.

Shuvalov, V.A., Klevanik, A.V., Sharkov, A.V., Kryukov, P.G., and Bacon, K.E. (1979c). Picosecond spectroscopy of photosystem I reaction centers. FEBS Lett. *107*, 313–316.

Sinnecker, S., Koch, W., and Lubitz, W. (2000). Bacteriochlorophyll *a* radical cation and anion—calculation of isotropic hyperfine coupling constants by density functional methods. Phys. Chem. Chem. Phys. *2*, 4772–4778.

Sinnecker, S., Koch, W., and Lubitz, W. (2002). Chlorophyll a radical ions: A density functional study. J. Phys. Chem. B *106*, 5281–5288.

Sirohiwal, A., Neese, F., and Pantazis, D.A. (2020). Protein matrix control of reaction center excitation in photosystem II. J. Amer. Chem. Soc. *142*, 18174–18190.

Sproviero, E.M., Gascón, J.A., McEvoy, J.P., Brudvig, G.W., and Batista, V.S. (2006). QM/MM models of the O_2-evolving complex of photosystem II. J. Chem. Theor. Comput *2*, 1119–1134.

Srinivasan, N., Chatterjee, R., Milikisiyants, S., Golbeck, J.H., and Lakshmi, K.V. (2011a). Effect of hydrogen bond strength on the redox properties of phylloquinones: a two-dimensional hyperfine sublevel correlation spectroscopy study of photosystem I. Biochemistry *50*, 3495–3501.

Srinivasan, N., and Golbeck, J.H. (2009). Protein-cofactor interactions in bioenergetic complexes: The role of the A_{1A} and A_{1B} phylloquinones in photosystem I. Biochim. Biophys. Acta *1787*, 1057–1088.

Srinivasan, N., Karyagina, I., Bittl, R., van der Est, A., and Golbeck, J.H. (2009). Role of the hydrogen bond from Leu722 to the A_{1A} phylloquinone in photosystem I. Biochemistry *48*, 3315–3324.

Srinivasan, N., Santabarbara, S., Rappaport, F., Carbonera, D., Redding, K., van der Est, A., and Golbeck, J.H. (2011b). Alteration of the H-bond to the A_{1A} phylloquinone in photosystem I: influence on the kinetics and energetics of electron transfer. J. Phys. Chem. B *115*, 1751–1759.

Stoll, S., Calle, C., Mitrikas, G., and Schweiger, A. (2005). Peak suppression in ESEEM spectra of multinuclear spin systems. J. Magn. Reson. *177*, 93–101.

Stoll, S., and Schweiger, A. (2006). EasySpin, a comprehensive software package for spectral simulation and analysis in EPR. J. Magn. Reson. *178*, 42–55.

Sun, J., Hao, S., Radle, M., Xu, W., Shelaev, I., Nadtochenko, V., Shuvalov, V., Semenov, A., Gordon, H., van der Est, A., and Golbeck, J.H. (2014). Evidence that histidine forms a

coordination bond to the A_{0A} and A_{0B} chlorophylls and a second H-bond to the A_{1A} and A_{1B} phylloquinones in M688HPsaA and M668HPsaB variants of *Synechocystis* sp. PCC 6803. Biochim. Biophys. Acta Bioenerg. *1837*, 1362–1375.

Sun, Y., Dai, Z., Wang, W., and Sun, Y. (2006). A DFT study on the electronic character of P_{700}^{+}. J. Theor. Comput. Chem. *05*, 733–741.

Taguchi, A.T., Baldansuren, A., and Dikanov, S.A. (2017). Basic and combination cross-features in X- and Q-band HYSCORE of the ^{15}N labeled bacteriochlorophyll a cation radical. Z. Phys. Chem. *231*, 725–743.

Thornber, J.P. (1975). Chlorophyll-proteins: Light-harvesting and reaction center components of plants. Annu. Rev. Plant Physiol. *26*, 127–158.

Umena, Y., Kawakami, K., Shen, J.R., and Kamiya, N. (2011). Crystal structure of oxygen-evolving photosystem II at a resolution of 1.9 A. Nature *473*, 55–60.

van der Est, A. (2006). Electron transfer involving phylloquinone in photosystem I. In Phototosystem I: The Light-Induced Plastocyanin:Ferredoxin Oxidoreductase, J.H. Golbeck, ed. (Springer), pp. 387–411.

van Doorslaer, S. (2017). Understanding heme proteins with hyperfine spectroscopy. J. Magn. Reson. *280*, 79–88.

Wasielewski, M.R., Fenton, J.M., and Govindjee. (1987). The rate of formation of $P_{700}^{+}-A_0^{-}$ in photosystem I particles from spinach as measured by picosecond transient absorption spectroscopy. Photosyn Res. *12*, 181–189.

Webber, A.N., and Lubitz, W. (2001). P_{700}: The primary electron donor of photosystem I. Biochim. Biophys. Acta Bioenerg. *1507*, 61–79.

Xu, W., Chitnis, P.R., Valieva, A., van der Est, A., Brettel, K., Guergova-Kuras, M., Pushkar, Y.N., Zech, S.G., Stehlik, D., Shen, G.Z., et al. (2003a). Electron transfer in cyanobacterial photosystem I - II. Determination of forward electron transfer rates of site-directed mutants in a putative electron transfer pathway prom A_0 through A_1 to F_X. J. Biol. Chem. *278*, 27876–27887.

Xu, W., Chitnis, P.R., Valieva, A., van der Est, A., Pushkar, Y.N., Krzystyniak, M., Teutloff, C., Zech, S.G., Bittl, B., Stehlik, D., et al. (2003b). Electron transfer in cyanobacterial photosystem I - I. Physiological and spectroscopic characterization of site-directed mutants in a putative electron transfer pathway from A_0 through A_1 to F_X. J. Biol. Chem. *278*, 27864–27875.

Yin, S., Dahlbom, M.G., Canfield, P.J., Hush, N.S., Kobayashi, R., and Reimers, J.R. (2007). Assignment of the Q_y absorption spectrum of photosystem I from *Thermosynechococcus elongatus* based on CAM-B3LYP calculations at the PW91-optimized protein structure. J. Phys. Chem. B *111*, 9923–9930.

STAR★METHODS

KEY RESOURCES TABLE

REAGENT or RESOURCE	SOURCE	IDENTIFIER
Bacterial and virus strains		
Wild-type *Synechocystis* sp. PCC 6803	Lab of John Golbeck	N/A
Δ*menB Synechocystis* sp. PCC 6803	Lab of John Golbeck	N/A
Biological samples		
Wild-type *Synechocystis* sp. PCC 6803 Photosystem I	Lab of John Golbeck	N/A
Δ*menB Synechocystis* sp. PCC 6803 Photosystem I	Lab of John Golbeck	N/A
Chemicals, peptides, and recombinant proteins		
n-dodecyl β-d-maltopyranoside (β-DDM)	Anatrace	D310; CAS: 69227-93-6
Tris	VWR	0497; CAS: 77-86-1
Glycerol	VWR	BDH1172; CAS: 56-81-5
Diethyl ether	Millipore	EX0190; CAS: 60-29-7
Ethanol	VWR	V1005; CAS: 64-17-5
Sucrose	EMD	SX1075; CAS: 57-50-1
Sodium Chloride	EMD	SX0420
Spectinomycin	Dot scientific	DSS23000; CAS 22189-32-9
Potassium Ferricyanide	Mallinckrodt	6913; 13746-66-2
Sodium Carbonate	VWR	0585; CAS: 497-19-8
Ferric Ammonium Citrate	MP	158040; CAS: 1185-57-5
Citric Acid	Aldrich	127; CAS: 77-92-9
Calcium Chloride	Research organics	1005C; CAS: 10035-04-8
Magnesium Sulfate Heptahydrate	Amresco	0662; CAS: 10034-99-8
Potassium Phosphate Dibasic	J.T. Baker	3246; CAS: 7778-77-0
Sodium Nitrate	J.T. Baker	3770; CAS: 7631-99-4
HEPES, Free Acid	J.T. Baker	4018; CAS: 7365-45-9
Triton X-100	Sigma	T9284; CAS: 9002-93-1
Sodium dithionite	Sigma-Aldrich	157953; CAS: 7775-14-6
Software and algorithms		
EasySpin 5.2	https://www.easyspin.org	N/A
MatLab	Mathworks.com	N/A
ORCA 4.2	orcaforum.kofo.mpg.de	N/A
Visual Molecular Dynamics (VMD) 1.9	NIH CENTER FOR MACROMOLECULAR MODELING & BIOINFORMATICS UNIVERSITY OF ILLINOIS AT URBANA-CHAMPAIGN	N/A

RESOURCE AVAILABILITY

Lead contact

Further information and requests for resources should be directed to and will be fulfilled by the Lead Contact, K. V. Lakshmi (lakshk@rpi.edu).

Materials availability

This study did not generate unique reagents. Requests for samples that were analyzed in this study can be directed to the Lead Contact, K. V. Lakshmi (lakshk@rpi.edu).

Data availability

Numerically simulated parameters in this study are available by contacting the lead contact, K. V. Lakshmi (lakshk@rpi.edu).

METHOD DETAILS

Preparation of photosystem I samples

PS I complexes were isolated and purified from wild-type (WT) and $\Delta menB$ *Synechocystis* sp. PCC 6803 similar to previously published procedures (Rögner et al., 1990; Johnson et al., 2000). Cells were grown at 30°C in β-HEPES medium under continuous illumination while bubbling 1% CO_2. The cells were harvested by centrifugation and lysed in a French pressure cell. The unbroken cells and debris were removed by centrifugation at 5,000 x g for 10 min at 4°C. Subsequently, the thylakoid membranes were pelleted by ultracentrifugation at 50,000 x g for 45 min at 4°C. Membranes were resuspended in 50 mM Tris 50 mM Tris·HCl buffer 10% glycerol at a pH of 8.3 and stored at –80°C until use. The thylakoid membranes were solubilized by adding 1% n-dodecyl β-d-maltopyranoside (β-DDM) in the dark at 4°C and the PS I complexes were isolated by a sucrose density gradient ultracentrifugation, using a gradient of 5% – 20% sucrose. The gradient was spun at r_{max} = 143K x g for 16 hours at 4°C. Trimers were collected from the first gradient from the dark green band at ~15% sucrose, after which the detergent and sucrose were removed using ultrafiltration over a 100 kDa membrane. PS I particles were pelleted in a second gradient of 5% – 20% sucrose that was spun at r_{max} = 175K x g for 16 hours at 4°C. The PS I was resuspended in 50 mM Tris·HCl buffer containing 0.05% β-DDM and 10% glycerol at a pH of 8.3. The samples were stored at –80°C until use.

Trapping of the $A_{0A}{}^{\cdot-}$ state

Cryogenic photo-accumulation of the $A_{0A}{}^{\cdot-}$ state requires inhibition of forward electron transfer to A_1. This was accomplished by removal of the phylloquinone cofactor occupying the A_1 site followed by chemical reduction of the [4Fe–4S] clusters of wild-type PS I. The phylloquinone in the A_1 site was removed by the treatment of PS I with water-saturated diethyl ether as described previously (Ikegami and Kato, 1975; Itoh et al., 1987, 2001; Ikegami et al., 2000). PS I particles were washed over a 100 kDa membrane to remove detergent and subsequently lyophilized. The lyophilized protein was treated with water saturated diethyl ether three times at 4°C to remove the pigments, spinning down the protein after each treatment. The protein was then resuspended in in 50 mM Tris·HCl buffer containing 0.05% β-DDM and 10% glycerol. The reduction of the [4Fe–4S] clusters was accomplished by the addition of 50 mM sodium dithionite under anaerobic conditions (Lakshmi et al., 1999). The $\Delta menB$ genetic variant of PS I was treated with 0.5% Triton X-100 to remove the plastoquinone in the A_1 site (Johnson et al., 2001) and the $A_0{}^{\cdot-}$ state of this sample yielded virtually identical spectral features to the water-saturated diethyl ether treated wild-type PS I (Figure S5). However, the data presented in this paper was obtained from water-saturated diethyl ether treated wild-type PS I as the $\Delta menB$ PS I sample treated with 0.5% Triton X-100 resulted in spectra with a lower signal-to-noise ratio due lower protein concentration. Prior to low-temperature illumination, the respective PS I samples were cooled in a dewar containing a dry ice/ethanol mixture at 220 K and after equilibration, the sample was illuminated for 1 min with 100 W of white light. The sample was rapidly frozen in liquid nitrogen in the dark after the illumination. The $P_{700}{}^{\cdot+}$ state was generated by chemical oxidation of wild-type PS I by the addition of 0.05 mM potassium ferricyanide (Lakshmi et al., 1999). The inherent ratio of A:B:2:1 for ET along the A- and B-branches, combined with experimental studies showcasing the difficulty in reducing $A_{1B}{}^{\cdot-}$ compared to $A_{1A}{}^{\cdot-}$ (Poluektov et al., 2005), suggests that $A_{0A}{}^{\cdot-}$ is the primary species being generated in this study. Therefore, contributions by $A_{0B}{}^{\cdot-}$ are expected to be minimal.

Pulsed electron paramagnetic resonance spectroscopy

The EPR spectra were obtained on a custom-built continuous-wave (*CW*)/pulsed X-band Bruker ELEXSYS 580 EPR spectrometer using a dielectric flex-line ER 4118-MD5 probe (Bruker BioSpin, Billerica, MA) and a dynamic continuous-flow cryostat CF935 (Oxford Instruments, Oxfordshire, U.K.).

The 2D ^{14}N and ^{1}H HYSCORE spectra of the $A_0{}^{\cdot-}$ and $P_{700}{}^{\cdot+}$ state of PS I were acquired at 80 K and 50 K, respectively, at a magnetic field position of 345.8 mT and 346.1 mT in the EPR spectrum (Figures 2 and S2, S3, S5, S7, and S8, respectively) which results in higher signal to noise of the 2D ^{14}N HYSCORE spectrum. For the 4-pulse HYSCORE sequence, the echo amplitude was measured using the pulse sequence ($\pi/2$–τ–$\pi/2$–t_1–π–t_2–$\pi/2$–τ–echo) with a τ value of 136 ns. The pulse length was 8 ns and 16 ns for the $\pi/2$- and π-pulse, respectively. The delays in the pulse sequence are defined as the difference in

the starting point of the pulses. The echo intensity was measured as a function of t_1 and t_2, where t_1 and t_2 were incremented in steps of 16 ns from an initial value of 40 ns and 32 ns, respectively. A total of 384 steps were used for each dimension. The 8 ns time difference between the initial value of t_1 and t_2 was set to account for the difference in length between the $\pi/2$- and π-pulse. This provided symmetric spectra in both dimensions. The unwanted echoes were eliminated by applying a 16-step phase cycling procedure.

The use of a 4-pulse HYSCORE sequence often results in the suppression of cross-peaks due to deep signal modulations from strongly coupled ^{14}N nuclei and the presence of unwanted inter-nuclear combination peaks that hinder the observation of some of the hyperfine interactions in both ESEEM and 2D HYSCORE experiments. Therefore, a 6-pulse HYSCORE sequence was also used for the acquisition of the 2D ^{14}N HYSCORE spectra of the $P_{700}^{\cdot+}$ state of PS I. For the 6-pulse HYSCORE sequence, the echo amplitude was measured with the pulse sequence ($\pi/2$-τ_1-π-τ_1-$\pi/2$-t_1-π-t_2-$\pi/2$-τ_2-π-τ_2-echo). The inter-pulse delays were defined as the difference between the starting points of the pulses. Equal amplitude pulses of 8 ns for $\pi/2$ and 16 ns for π were used to record a 256 x 256 matrix. The 8 ns time difference between the initial value of the time delays, t_1 and t_2, and the $\pi/2$ and π pulses was used to account for the difference in length between the $\pi/2$ and π-pulses to obtain symmetric spectra. The echo intensity was measured as a function of t_1 and t_2, where t_1 and t_2 were incremented in steps of 24 ns. The blind spot pattern in a 6-pulse 2D HYSCORE spectrum is determined by the τ_1 and τ_2 delays. Hence, the τ_1 and τ_2 delay was set to 32 ns and 100 ns, respectively, to avoid blind spots and resonator ring down. The application of an 8-step phase cycling procedure was used to eliminate the unwanted echoes. The use of a 6-pulse HYSCORE sequence led to the observation of additional cross-peaks that were not detected in the 4-pulse HYSCORE experiment (see supplemental information for experimental and simulated spectra).

The time domain 4-pulse and 6-pulse 2D HYSCORE data was processed using MATLAB R2018b. A third order polynomial baseline was subtracted from the resulting time-domain spectra. The corrected spectra were zero-filled to obtain a [2048 x 2048] matrix and Fourier transformed using a Fast Fourier Transformation (FFT) algorithm. The frequency domain spectra were plotted as the amplitude (absolute value) of the 2D frequency components. Numerical simulations of the experimental 2D HYSCORE spectra using the hyperfine parameters obtained from the spectra analysis were performed using the "saffron" function of the EasySpin software package (Stoll and Schweiger, 2006).

DFT calculations

The DFT calculations of the primary acceptor anion, $A_0^{\cdot-}$, and primary donor cation, $P_{700}^{\cdot+}$, were performed with a B3LYP functional and EPR-II basis set using the software program, ORCA 4.0 (Neese, 2012, 2018). The coordinates for the atoms in each computational model were derived from the X-ray coordinates of Photosystem I from *Thermosynechococcus elongatus* (Jordan et al., 2001). The initial computational model for the $A_0^{\cdot-}$ state was comprised of the $Chl_{3A}^{\cdot-}$ anion radical with the constituent atoms of the Chl_{3A} cofactor. The model was systematically expanded to include the axial Met ligand, $Met688_{PsaA}$, that is coordinated to the central Mg^{2+} ion of the Chl_{3A} cofactor and the hydrogen-bonded Tyr residue, $Tyr696_{PsaA}$, A_{1A}, $Chl_{2A/2B}$, $Chl_{1A/1B}$ cofactors and their respective axial ligands, namely, water molecules and His residues. To limit the size of the computational model in the calculations, the isoprenoid substituent of the Chl_{3A}, $Chl_{2A/2B}$ and $Chl_{1A/1B}$ cofactors was truncated in all of the calculations to contain 8 carbon atoms. The computational model for $P_{700}^{\cdot+}$ contained the constituent atoms of the $Chl_{1A/1B}$ cofactors with the respective axial histidine ligand and the isoprenoid substituent of $Chl_{1A/1B}$ cofactor was truncated to contain 5 carbon atoms. All of the geometry optimizations were carried out at the B3LYP level of theory with the DZVP basis set to expand the Kohn-Sham orbitals. For the B3LYP single point calculations on the optimized structures, the EPR-II basis set was used for the lighter atoms in the models, while the 6-31G(d) basis set was incorporated for the Mg^{2+} ion. The RIJCOSX approximation was employed in conjunction with the CPCM solvent model with a dielectric (ε) of 4.0 to approximate the surrounding protein environment. The electron spin density distribution for each structure was visualized in the molecular modeling and visualization program, Visual Molecular Dynamics (VMD).